

Adjoint inversion of Chinese non-methane volatile organic compound emissions using space-based observations of formaldehyde and glyoxal

Hansen Cao¹, Tzung-May Fu^{1,*}, Lin Zhang¹, Daven K. Henze², Christopher Chan Miller³, Christophe Lerot⁴, Gonzalo González Abad³, Isabelle De Smedt⁴, Qiang Zhang⁵, Michel van Roozendael⁴, François Hendrick⁴, Kelly Chance³, Jie Li⁶, Junyu Zheng⁷, Yuanhong Zhao¹

¹Department of Atmospheric and Oceanic Sciences and Laboratory for Climate and Ocean-Atmosphere Studies, School of Physics, Peking University, Beijing, 100871, China

²Department of Mechanical Engineering, University of Colorado, Boulder, USA

³Atomic and Molecular Physics Division, Harvard-Smithsonian Center for Astrophysics, Cambridge, Massachusetts, USA

⁴Belgian Institute for Space Aeronomy, Brussels, Belgium

⁵Center for Earth System Science, Tsinghua University, Beijing, China

⁶Institute of Atmospheric Physics, Chinese Academy of Sciences, Beijing, China

⁷College of Environmental Science and Engineering, South China University of Technology, Guangzhou, China

Correspondence to: Tzung-May Fu (tmfu@pku.edu.cn)

Abstract. We used the GEOS-Chem model and its adjoint to quantify Chinese non-methane volatile organic compound (NMVOC) emissions for the year 2007, using the tropospheric column concentrations of formaldehyde and glyoxal observed by the Global Ozone Monitoring Experiment-2A (GOME-2A) instrument and the Ozone Monitoring Instrument (OMI) as quantitative constraints. We conducted a series of inversion experiments using different combinations of satellite observations to explore their impacts on the top-down emission estimates. Our top-down estimates for Chinese annual total NMVOC emission were 30.7 to 49.5 (average 41.9) Tg y⁻¹, including 16.4 to 23.6 (average 20.2) Tg y⁻¹ from anthropogenic sources, 12.2 to 22.8 (average 19.2) Tg y⁻¹ from biogenic sources, and 2.08 to 3.13 (average 2.48) Tg y⁻¹ from biomass burning. In comparison, the *a priori* estimate for Chinese annual total NMVOC emission was 38.3 Tg y⁻¹, including 18.8 Tg y⁻¹ from anthropogenic sources, 17.3 Tg y⁻¹ from biogenic sources, and 2.27 Tg y⁻¹ from biomass burning. The simultaneous use of glyoxal and formaldehyde observations helped distinguish the NMVOC species from different sources and was

essential in constraining anthropogenic emissions. Our four inversion experiments consistently showed that the Chinese anthropogenic emissions of NMVOC precursors of glyoxal were larger than the *a priori* estimates. Our top-down estimates for Chinese annual emission of anthropogenic aromatics (benzene, toluene, and xylene) ranged from 5.5 to 7.9 Tg y⁻¹, 2% to 46% larger than the estimate of the *a priori* emission inventory (5.4 Tg y⁻¹). Three out of our four inversion experiments indicated that the seasonal variation of Chinese NMVOC emissions was significantly stronger than indicated in the *a priori* inventory. Model simulations driven by the average of our top-down NMVOC emission estimates (which had a stronger seasonal variation than the *a priori*) showed that surface afternoon ozone concentrations over eastern China increased by 1-8 ppb in June and decreased by 1-10 ppb in December relative to the simulations using the *a priori* emissions and were in better agreement with measurements. We concluded that the satellite observations of formaldehyde and glyoxal together provided quantitative constraints on the emissions and source types of NMVOCs over China and improved our understanding on regional chemistry.

1 Introduction

Non-methane volatile organic compounds (NMVOCs) are emitted into the atmosphere from surface anthropogenic, biogenic, and biomass burning sources. NMVOCs are precursors to tropospheric ozone and secondary organic aerosols, both of which are climate forcers and major air pollutants. NMVOC also affect the oxidation capacity of the atmosphere, which in turn changes the lifetimes of greenhouse gases and other pollutants. It is thus crucial to quantify NMVOC emissions in order to understand their impacts on atmospheric chemistry and climate on both global and regional scales. Here we used satellite observations and a chemical transport model to constrain NMVOC emissions from China and assessed their impacts on seasonal surface ozone.

Emissions of trace species are traditionally estimated in a “bottom-up” manner using activity data and emission factors, but these bottom-up estimates are sometimes susceptible to large uncertainties. This is especially true for NMVOC emissions in developing countries such as China, because (1) a wide range of species, source activities, and technologies are involved (Q. Zhang et al., 2009; Kurokawa et al., 2013; Li et al., 2014; Qiu et al., 2014), (2) locally-representative emission factors are often not

measured (Wei et al., 2008; Zhao et al., 2011), and (3) reliable activity data are often incomplete, particularly for small-scale industries, residential activities, and agricultural waste burning (Q. Zhang et al., 2009). Bottom-up estimates for Chinese total annual NMVOC emissions for the years 2005 to 2012 ranged from 31 to 57 Tg y⁻¹ (Guenther et al., 2006; Bo et al., 2008; Q. Zhang et al., 2009; van der Werf et al., 2010, 2017; Cao et al., 2011; Huang et al., 2012; Kurokawa et al., 2013; Li et al., 2014; Stavrakou et al., 2014; Sindelarova et al., 2014; Wu et al., 2016; Huang et al., 2017; Granier et al., 2017). Such large uncertainties in the emission estimates of Chinese NMVOCs have led to great difficulty in evaluating their impacts on regional chemistry (Han et al., 2013; Wang et al., 2014).

A complementary, “top-down” approach for quantifying emissions uses observations of the targeted species or its chemical derivatives, combined with a chemical transport model acting as a transfer function, to invert for the fluxes of the targeted species. In particular, tropospheric column concentrations of formaldehyde, retrieved from satellite UV-backscatter measurements, have been used to constrain NMVOC emissions. Formaldehyde is produced at high yields during the oxidation of many NMVOC species (Millet et al., 2006) and also emitted directly from anthropogenic and biomass burning activities (Akagi et al., 2011; Li et al., 2017). Early inversions of satellite-observed formaldehyde columns mostly focused on areas where the local NMVOC fluxes were dominated by biogenic sources during the growing season and in the absence of substantial biomass burning, such as the southeast U.S. (Palmer et al., 2003, 2006; Millet et al., 2006, 2008), Europe (Dufour et al., 2009; Curci et al., 2010), the Amazon (Barkley et al., 2008, 2009, 2013), and Africa (Marais et al., 2012, 2014a). These studies showed that the observed local enhancements of formaldehyde column concentrations can be used to quantitatively constrain local biogenic NMVOC fluxes.

In other areas, the NMVOC emissions from various sources may be comparable in magnitudes. Several studies constrained the NMVOC emissions from multiple sources over such areas by analyzing the spatiotemporal variability of the observed formaldehyde columns (Shim et al., 2005; Fu et al., 2007; Stavrakou et al., 2009b; Curci et al., 2010; Gonzi et al., 2011; Marais et al., 2014b; Zhu et al., 2014). Fu et al. (2007) analyzed the spatial and seasonal variation of the formaldehyde column observations from the Global Ozone Monitoring Experiment (GOME) over East and South Asia. They showed that, during the early 2000s, Chinese reactive NMVOC fluxes from biogenic, anthropogenic, and biomass

93 burning sources were 3, 1.2, and 8.8 times their respective bottom-up estimates at that time. In
94 particular, Fu et al. (2007) found a large, annually-recurring NMVOC source over the North China
95 Plain (NCP) in June, which they attributed to crop residue burning after the local harvest of winter
96 wheat. However, these top-down studies using only formaldehyde as constraints relied exclusively on
97 bottom-up activity statistics to differentiate between NMVOC source types.

98
99 More recently, satellite measurements of tropospheric glyoxal columns emerged as an additional
100 constraint on NMVOC emissions (Stavrakou et al., 2009a). Like formaldehyde, glyoxal is produced
101 during the oxidation of many NMVOCs (including most importantly isoprene), as well as emitted
102 directly from biomass burning (Fu et al., 2008; Myriokefalitakis et al., 2008). In particular, glyoxal is
103 produced at high yields at the initial ring-cleaving stage during the oxidation of aromatics (Volkamer,
104 2001; Nishino et al., 2010), which are mainly anthropogenic. In contrast, the production of
105 formaldehyde from the oxidation of aromatics is further downstream and thus spatially diffuse
106 (Volkamer, 2001). As such, simultaneous analyses of formaldehyde and glyoxal observations can help
107 differentiate between biogenic and anthropogenic NMVOC emissions. Stavrakou et al. (2009a)
108 pioneered a two-compound inversion using tropospheric glyoxal and formaldehyde column
109 observations from the Scanning Imaging Absorption spectrometer for Atmospheric CHartography
110 (SCIAMACHY) satellite instrument to constrain the global sources of glyoxal. They estimated that the
111 anthropogenic NMVOC fluxes over East Asia for the year 2005 were a factor of 2 to 3 larger than the
112 bottom-up estimates of the Emission Database for Global Atmospheric Research (EDGAR, v3.3)
113 inventory (Olivier et al., 2001, 2002) and the REanalysis TROpospheric (RETRO) emission inventory
114 (Schultz et al., 2007). In addition, they inferred a large missing source of glyoxal over the global
115 continents, which they attributed to production from an unknown biogenic precursor.

116
117 Over eastern China, Liu et al. (2012) showed that the glyoxal column concentrations observed by
118 SCIAMACHY in August 2007 was more than twice the simulated glyoxal columns using the
119 bottom-up emission inventory developed by Q. Zhang et al. (2009). Over the Pearl River Delta area
120 (PRD) in southern China, the discrepancy was at least a factor of three. They suggested that the
121 missing glyoxal source over eastern China was anthropogenic, on the basis that the anomalous glyoxal
122 columns observed by SCIAMACHY (relative to the glyoxal columns simulated by their model) were

spatially correlated with anthropogenic NO_x emissions. They estimated the Chinese anthropogenic aromatics emission to be 13.4 Tg y⁻¹, which was six times the 2.4 Tg y⁻¹ anthropogenic aromatic flux estimated by Q. Zhang et al. (2009). In contrast, Chan Miller et al. (2016) simulated the formaldehyde and glyoxal column concentrations over the Pearl River Delta area (PRD) in southern China for the years 2006 and 2007 using the same inventory developed by Q. Zhang et al. (2009). They found that their simulated formaldehyde columns were consistent with the OMI formaldehyde observations, while their simulated glyoxal columns were lower than OMI observations by only 40%. They attributed the high anthropogenic aromatics emission estimate by Liu et al. (2012) in part to a regional high-bias in the SCIAMACHY data, and in part to the lower glyoxal yields from aromatics oxidation used in Liu et al. (2012).

One limitation in the use of satellite observations of formaldehyde and glyoxal for constraining NMVOC sources is their inherent uncertainty. Several studies have compared GOME-2A and OMI formaldehyde column observations against aircraft or ground-based measurements at a few locations around the world (De Smedt et al., 2015; Lee et al., 2015; Wang et al., 2017; Zhu et al., 2016). Zhu et al. (2016) compared the GOME-2A-observed formaldehyde column concentrations over the Southeast U.S. in summer 2013 against aircraft measurements and found the satellite measurements to be too low by a factor of approximately 1.7. Chan Miller et al. (2017) found that glyoxal column concentrations observed by OMI were lower than the aircraft measurements over the Southeast U.S. in summer 2013 by a factor of 1.5. Wang et al. (2017) compared the bi-monthly mean GOME-2A and OMI formaldehyde column concentrations retrieved by De Smedt et al. (2012, 2015) against ground-based multi-axis differential optical absorption spectroscopy (MAX-DOAS) measurements at a rural site in eastern China. They found that both satellite retrievals were systematically lower than the ground-based measurements by approximately 20%. These studies highlighted the potential impacts on top-down NMVOC emission estimates due to uncertainty associated with satellite retrievals.

In this study, we used satellite retrievals of both formaldehyde and glyoxal, along with a chemical transport model and its adjoint, to constrain NMVOC emissions from China for the year 2007. We conducted sensitivity experiments to evaluate the impacts on the top-down estimates due to different

satellite observations, with the goal of bracketing a probable range of top-down estimates. Finally, we examined the impacts of our top-down NMVOC emission estimates on surface air quality over China.

2 Model and data

2.1 The GEOS-Chem model and its adjoint

We updated the GEOS-Chem global 3D chemical transport model (version 8.2.1) to simulate the emission, transport, chemistry, and deposition of NMVOCs, as well as the resulting formaldehyde and glyoxal column concentrations for the year 2007. The use of an older version of the GEOS-Chem forward model was necessary because, at the time of our study, the GEOS-Chem adjoint (version 34) was based on this older version. However, we updated the NMVOC chemical schemes (described below) and corrected several model errors in both our forward model and its adjoint by following the progress of the forward model up to version 10.1. GEOS-Chem was driven by the assimilated meteorological data from the NASA Goddard Earth Observing System (GEOS-5) (Bey et al., 2001). To drive our simulations, the horizontal resolution of GEOS-5 data was downgraded from its native $2/3^\circ$ longitude \times $1/2^\circ$ latitude to 5° longitude \times 4° latitude. The number of vertical levels was reduced from 72 to 47 by merging layers in the stratosphere. The lower 2 km of the atmosphere was resolved by 14 levels. The temporal resolution of GEOS-5 data into GEOS-Chem is 3 h for atmospheric variables and 1 h for surface variables.

We updated the dicarbonyl chemical mechanism in GEOS-Chem developed by Fu et al. (2008), which in turn was originally adapted from the Master Chemical Mechanism (MCM) version 3.1 (Jenkin et al., 1997; Saunders et al., 2003). Table S1 lists the yields of formaldehyde and glyoxal from the OH-oxidation of NMVOC precursors in our updated chemical mechanism. The lumped NMVOC precursors of formaldehyde in our mechanism included ethane, propane, $\geq C_4$ alkanes, ethene, $\geq C_3$ alkenes, benzene, toluene, xylenes, isoprene, monoterpenes, acetone, hydroxyacetone, methylglyoxal, glycolaldehyde, acetaldehyde, 2-methyl-3-buten-2-ol, methyl ethyl ketone, methanol, and ethanol (lumped into $\geq C_4$ alkanes). The lumped NMVOC precursors of glyoxal in our mechanism included ethene, ethyne, benzene, toluene, xylenes, isoprene, monoterpenes, glycolaldehyde, and 2-methyl-3-buten-2-ol (MBO). Hereinafter we focused our discussion on these NMVOC precursors

only, as their emissions may be constrained by formaldehyde and glyoxal observations.

The OH-oxidation of isoprene is a major source of both formaldehyde and glyoxal over China (Fu et al., 2007, 2008; Myriokefalitakis et al., 2008). We replaced the isoprene photochemical scheme with that used in GEOS-Chem v10.1, which included updates from Paulot et al. (2009a,b) and Mao et al. (2013). In this updated scheme, oxidation of isoprene by OH under high-NO_x conditions produces formaldehyde and glyoxal at yields of 0.436 molecules per C and 0.0255 molecules per C, respectively (Table S1), mainly via the RO₂+NO pathways. Under low-NO_x conditions, oxidation of isoprene by OH produces formaldehyde and glyoxal at yields of 0.38 molecules per C and 0.073 molecules per C, respectively (Table S1), via both RO₂+HO₂ and RO₂-isomerization reactions. Li et al. (2016) implemented this same isoprene photochemical scheme in a box model and compared the productions of formaldehyde and glyoxal from isoprene oxidation with those in the MCM version 3.3.1 (Jenkin et al., 2015). They showed that the production pathways and yields of formaldehyde and glyoxal were similar in the two schemes under the high-NO_x conditions typical of eastern China.

We updated the molar yields of glyoxal from the OH oxidations of benzene (33.3%), toluene (26.2%), and xylenes (21.0%) following the latest literature (Arey et al., 2009; Nishino et al., 2010). These new molar yields were higher than those used in Fu et al. (2008) (based on averaged yields in the literature: 25.2% for benzene, 16.2% for toluene, and 15.6% for xylenes) but still lower than those used by Chan Miller et al. (2016) (75% for benzene, 70% for toluene, and 36% for xylenes), which were taken from the aromatic chemical scheme in MCM version 3.2 (Jenkin et al., 2003; Bloss et al., 2005). In MCM version 3.2, more than half of the glyoxal from aromatics oxidation were produced during second- and later-generation photochemistry, but such productions are with limited experimental support and uncertain (Bloss et al., 2005).

Formaldehyde and glyoxal in the GEOS-Chem model were both removed by photolysis, as well as dry and wet deposition (Fu et al., 2008). We updated the Henry's law constant for glyoxal from $3.6 \times 10^5 \times \exp[7.2 \times 10^3 \times (1/T-1/298)]$ (Fu et al., 2008) to $4.19 \times 10^5 \times \exp[(62.2 \times 10^3/R) \times (1/T-1/298)]$ (Ip et al., 2009) and added the dry deposition of formaldehyde, glyoxal, methyglyoxal and glycolaldehyde on leaves (Mao et al., 2013). In addition, we assumed that glyoxal was reactively uptaken by wet aerosols

and cloud droplets with an uptake coefficient $\gamma = 2.9 \times 10^{-3}$ (Liggio et al., 2005; Fu et al., 2008). All other physical and chemical processes in our forward model were as described in Fu et al. (2008).

For the forward model described above, we developed the adjoint by modifying the standard GEOS-Chem adjoint (version 34) (Henze et al., 2007). We used the Kinetic PreProcessor (KPP) (Daescu et al., 2003; Sandu et al., 2003) to construct the adjoint of the updated photochemical mechanism. Adjoint algorithms were updated to include the emission and deposition processes of formaldehyde and glyoxal precursors. The aqueous uptake rate of glyoxal by wet aerosols was a function of the ambient glyoxal concentration and the total wet aerosol surface area (Fu et al., 2008). We linearized this uptake process in the backward integrations by using the archived wet aerosol surface areas from the forward simulations.

We verified the adjoint model mathematically in two ways. Firstly, we used the adjoint model to calculate the sensitivities of global glyoxal and formaldehyde burdens to biogenic isoprene and anthropogenic xylenes emissions, respectively, and found that the results reproduced the calculated sensitivities from the forward model (Figure S1). Secondly, we used a set of bottom-up NMVOC emission inventories (Section 2.2) to drive the forward model and took the resulting global tropospheric formaldehyde and glyoxal column concentrations as pseudo observations. We then used the pseudo observations of formaldehyde and glyoxal to successfully optimize back to the bottom-up NMVOC emission estimates over high-emission areas from an initial guess that was five times larger (Figure S2). These experiments demonstrated the usefulness of the adjoint model for the inversion of NMVOCs emissions.

2.2 *A priori* emission estimates of Chinese NMVOCs

As a starting point for our inversion, we compiled the *a priori* Chinese NMVOC emission estimates from recent bottom-up emission inventories. Table 1 summarizes the annual total of these *a priori* emission estimates and their associated uncertainties.

The *a priori* biogenic NMVOC emissions from China and from the rest of the world were calculated

with the MEGAN v2.0 algorithm (Guenther et al., 2006) and dependent on temperature, shortwave radiation, and monthly mean leaf area index. Previous top-down studies suggested that MEGAN overestimates global biogenic methanol by a factor of two to three (Stavrakou et al., 2011; Wells et al., 2012). We scaled our global biogenic methanol emissions to the value (100 Tg y⁻¹) reported by Stavrakou et al. (2011) to be the *a priori* in this study. The contributions of Chinese biogenic ethanol to formaldehyde are expected to be low due to its small emissions (Guenther et al., 2012); thus the Chinese biogenic ethanol emissions were neglected in this study. The resulting annual total biogenic NMVOC emissions over China for the year 2007 was 17.3 Tg y⁻¹, including 7.5 Tg y⁻¹ of isoprene, 4.6 Tg y⁻¹ of methanol, and 5.2 Tg y⁻¹ of other species (including monoterpenes, ethene, acetone, ≥C₃ alkenes, and MBO). Previous estimates of Chinese biogenic isoprene emissions ranged from 5.8 to 9.9 Tg y⁻¹ (Guenther et al., 2006; Sindelarova et al., 2014; Stavrakou et al., 2014, 2015, 2017). Based on this range, we estimated the uncertainty of the *a priori* biogenic emissions over China to be ±55%.

The *a priori* emissions for Chinese anthropogenic NMVOCs were from the Multi-resolution Emission Inventory for China inventory (MEIC, <http://meicmodel.org>) (Li et al., 2014, 2017), which was developed at 0.25 °×0.25 °resolution for the year 2010. The MEIC inventory, including emissions from industry, transportation, power generation and residential activities, was compiled using monthly Chinese provincial activity data and a combination of Chinese and western emission factors. The estimated Chinese annual anthropogenic emission of NMVOCs was 18.8 Tg y⁻¹, including 63% from industries, 26% from residential activities, 10% from transportation, and 1% from power generation. The estimated annual Chinese anthropogenic emission of aromatics was 5.4 Tg y⁻¹, including 73% from industries, 15% from residential activities, 9% from transportation, and 3% from power generation. Previous estimates of Chinese anthropogenic NMVOC emissions for the years 2005 to 2012 ranged from 12.7 to 35.5 Tg y⁻¹, with aromatics emissions ranging from 2.4 to 13.4 Tg y⁻¹ (Bo et al., 2008; Q. Zhang et al., 2009; Cao et al., 2011; Liu et al., 2012; Kurokawa et al., 2013; Li et al., 2014, 2017; Stavrakou et al., 2015; Wu et al., 2016; Huang et al., 2017; Granier et al., 2017). We therefore estimated the uncertainty for the *a priori* Chinese anthropogenic NMVOC emission estimates to be a factor of two. As such, we did not scale the MEIC Chinese NMVOC emissions to the year 2007, because the uncertainty in the emission estimates were much larger than the differences in emissions between the years 2007 and 2010 (Chinese anthropogenic NMVOC emissions increased 14% from

2006 to 2010 according to Li et al, 2017). The spatial distribution of Chinese anthropogenic NO_x emissions were from the MEIC inventory for the year 2010 (Li et al., 2017) but scaled to the year 2007 levels using top-down constraints from the GOME-2A NO₂ observations (Mijling et al., 2013). Anthropogenic NMVOC emissions for the rest of the Asia were from Li et al. (2017) for the year 2010. Anthropogenic emissions for Europe, U.S., and the rest of the world were from the European Monitoring and Evaluation Programme inventory (Vestreng, 2003), the U.S. EPA 2005 National Emission Inventory (<https://www.epa.gov/air-emissions-inventories/national-emissions-inventory-nei>), and the EDGAR inventory (version 2.0) (Olivier et al., 1999), respectively, and scaled to the year 2007 using CO₂ emissions (van Donkelaar et al., 2008).

Post-harvest, in-field burning of crop residue has been recognized as a large seasonal source of NMVOCs in China (Fu et al., 2007; Huang et al., 2012; Liu et al., 2015; Stavrakou et al., 2016). These emissions from crop residue fires have been severely underestimated in inventories based on burned area observations from satellites, such as the Global Fire Emissions Database version 3 (GFED3, van der Werf et al., 2010). The recent Global Fire Emissions Database version 4 (GFED4, van der Werf et al., 2017) included small fires by scaling burned area with satellite fire pixel observations, but the resulting Chinese NMVOC emission estimate from biomass burning (0.91 Tg y⁻¹) was still much lower than the bottom-up inventory by Huang et al. (2012). Huang et al. (2012) estimated the Chinese CO emission from crop residue burning to be 4.0 Tg y⁻¹, based on MODIS daily thermal anomalies, Chinese provincial burned biomass data, and emission factors from Akagi et al. (2011). We scaled this CO flux using speciated NMVOC emission factors from crop residue burning from the literature (Hays et al., 2002; Akagi et al., 2011) and then multiplied the resulting NMVOC flux estimate by two. The reason for doubling the scaled NMVOC flux was that the emission factors for many NMVOC species were not measured, such that the sum of the speciated NMVOC emission factors was only half of the total NMVOC emission factor (Akagi et al., 2011). This difference may partially explain why the formaldehyde inversion study by Stavrakou et al. (2016) found that Huang et al. (2012) underestimated the NMVOC fluxes from crop fires over the North China Plain (NCP) in June by at least a factor of two.

Our resulting *a priori* estimate for Chinese annual NMVOC emissions from biomass burning was 2.27

Tg y⁻¹, including 1.80 Tg y⁻¹ from crop residue burning (obtained by scaling Huang et al., 2012 as described above) and 0.47 Tg y⁻¹ from other types of biomass burning activities from GFED3 (van der Werf et al., 2010). Previous estimates of Chinese NMVOC emissions from biomass burning for the years 2000 to 2012 ranged widely from 0.47 to 5.1 Tg y⁻¹ (Fu et al., 2007; van der Werf et al., 2010, 2017; Wiedinmyer et al., 2011; Huang et al., 2012; Liu et al., 2015; Stavrakou et al., 2015, 2016). We therefore estimated the uncertainty of the *a priori* Chinese biomass burning NMVOC flux to be a factor of three. Biomass burning emissions from the rest of the world were from GFED3 (van der Werf et al., 2010).

Figure 1 (a)-(d) show the spatial distribution of the *a priori* Chinese NMVOC emissions from biomass burning, anthropogenic, biogenic, and total sources, respectively. Biomass burning emissions were highest over the NCP and southwest China, reflecting the strong emissions from crop residue burning over the NCP in June and over southwest China during February to April, respectively. Chinese anthropogenic and biogenic NMVOC sources were both stronger in the east than in the west, reflecting the co-location of dense population and vegetation in the east. The highest biogenic NMVOC emissions were over southern China, due to the combined modulation by vegetation densities, temperature, and sunlight. Anthropogenic NMVOC fluxes exceeded 10³ kg km⁻² y⁻¹ throughout the industrialized and densely populated eastern China, with the highest fluxes over the NCP and around the Yantze River Delta area.

Figure 2 shows the seasonal variation of the *a priori* Chinese NMVOC emissions. The *a priori* anthropogenic NMVOC fluxes were larger during the cold months and lower during the warm months, driven by the seasonal strengths of industrial and residential activities (Li et al., 2017). The *a priori* biogenic NMVOC fluxes showed the opposite seasonal pattern, with 65% of the total annual flux emitted in summer (June to August). The *a priori* biomass burning NMVOC source was relatively small, except when it peaked due to post-harvest burning over the NCP in June and over southwest China in spring. As a result, the *a priori* Chinese NMVOC emissions were predominantly anthropogenic in winter but mainly biogenic in summer. During the transition seasons of spring and fall, the anthropogenic, biogenic, and biomass burning contributions were comparable.

2.3 Formaldehyde and glyoxal column concentrations observed by GOME-2A and OMI

We used the monthly mean tropospheric formaldehyde and glyoxal column concentrations retrieved from the Global Ozone Monitoring Experiment-2A (GOME-2A) instrument and the Ozone Monitoring Instrument (OMI) for the year 2007 to constrain Chinese NMVOC sources. The four sets of satellite retrievals used in this study are briefly described below; further technical details are summarized in Table S2.

The native GOME-2A pixel vertical column densities (VCDs) of formaldehyde and glyoxal were retrieved by De Smedt et al. (2012) and Lerot et al. (2010), respectively. Pixel slant column densities (SCDs) of formaldehyde and glyoxal were retrieved in the 328.5-346 nm and 435-460 nm windows, respectively, using the Differential Optical Absorption Spectroscopy (DOAS) technique (Platt et al., 1979). Previous glyoxal SCD retrievals often showed biases over remote tropical oceans due to absorption from liquid water (Wittrock et al., 2006; Vrekoussis et al., 2010). This bias was corrected in Lerot et al. (2010) by explicitly accounting for liquid water absorption during the DOAS fitting. Pixel SCDs were then converted into VCDs using air mass factors (AMF), which was calculated using Linearized Discrete Ordinate Radiative Transfer model (LIDORT) (Spurr, 2008) and trace gas profiles simulated by the IMAGES v2 model (Stavrou et al., 2009b). The native pixel VCDs were gridded to daily means at $0.25^{\circ} \times 0.25^{\circ}$ resolution (De Smedt et al., 2012; Lerot et al., 2010). We further averaged the daily means to monthly means at 5° longitude \times 4° latitude resolution. The retrieval errors of the spatially-and-temporally averaged VCDs were estimated to be 30%-40% for formaldehyde and 40% for glyoxal, due to a combination of errors associated with the SCD retrievals, the reference sector correction, the *a priori* profile, and the AMFs (De Smedt et al., 2012; Lerot et al., 2010).

The OMI native pixel VCDs of formaldehyde and glyoxal were retrieved by González Abad et al. (2015) and Chan Miller et al. (2014), respectively. Pixel SCDs were retrieved by directly fitting the absorption spectra in the 328.5 – 356.5 nm (formaldehyde) and 435 – 461 nm (glyoxal) windows, respectively (Chance, 1998; Chan Miller et al., 2014). Pixel SCDs were then converted to VCDs using AMF calculated with a linearized vector discrete ordinate radiative transfer model, VLIDORT (Spurr,

2006), and trace gas profiles simulated by the GEOS-Chem model (González Abad et al., 2015). Liquid water absorption was also explicitly calculated for the glyoxal retrieval (Chan Miller et al., 2014). The typical uncertainties of OMI-observed pixel VCDs over polluted areas were estimated to be 30% to 45% for formaldehyde and 100% for glyoxal (González Abad et al., 2015; Chan Miller et al., 2014). The native pixel VCDs were averaged to monthly means at 5° longitude \times 4° latitude resolution. For glyoxal, we further removed VCDs with signal-to-uncertainty ratios less than 100%. We assumed the retrieval uncertainty of monthly mean OMI formaldehyde and glyoxal VCDs at $4^\circ \times 5^\circ$ resolution to be 40% and 100%, respectively.

To remove global systematic biases in the satellite observations, we aligned the observed monthly mean VCDs over remote reference areas to those simulated by the GEOS-Chem model (sampled at satellite overpass time) using the *a priori* NMVOC emissions. The remote Pacific (140° - 160° W, 90° S- 90° N) was chosen as the reference area for formaldehyde (Palmer et al., 2003, 2006; Fu et al., 2007; González Abad et al., 2015). The Sahara desert (20° - 30° N, 10° W- 30° E), where the interference from liquid water absorption was minimal, was chosen as the reference area for glyoxal (Chan Miller et al., 2014). The justification for performing the alignment was two-fold: firstly, the formaldehyde and glyoxal VCDs over these remote reference areas were small and well simulated by the model (Fu et al., 2007; Chan Miller et al., 2014). The removed biases over the remote areas were less than 20% and 10% of the typical formaldehyde ($>4 \times 10^{15}$ molecule cm^{-2}) and glyoxal ($>2 \times 10^{14}$ molecule cm^{-2}) monthly mean VCDs observed over eastern China, respectively. More importantly, our inversion was performed over China only, assuming that the *a priori* NMVOC emissions for the rest of the world were unbiased. As will be seen in Sections 3 and 4, the optimization of NMVOC sources were predominantly driven by local formaldehyde and glyoxal enhancements produced by relatively short-lived NMVOCs.

2.4 Inversion experiments using the GEOS-Chem adjoint

We used the GEOS-Chem model to perform Bayesian inversions on Chinese NMVOC emissions, using satellite observations of formaldehyde and glyoxal over China and the *a priori* emission estimates as constraints. The inversion minimized a cost function, $J(\mathbf{x})$, over China (Rodgers, 2000):

$$J(\mathbf{x}) = \gamma \bullet (\mathbf{x} - \mathbf{x}_a) S_a^{-1} (\mathbf{x} - \mathbf{x}_a) + (\mathbf{F}(\mathbf{x}) - \mathbf{y}) S_o^{-1} (\mathbf{F}(\mathbf{x}) - \mathbf{y}) \quad \text{Eq. (1)}$$

The first and second terms on the right-hand-side of Eq. (1) represented the penalty error and the prediction error, respectively. \mathbf{x} , which we sought to optimize, was the vector of scale factors (for each NMVOC species from each emission sector and for each grid) applied to the *a priori* emissions. \mathbf{x}_a was a unit vector applied to the *a priori* NMVOC emission estimates. \mathbf{y} was the vector of satellite-observed monthly mean VCDs of the targeted tracer (formaldehyde and/or glyoxal). $\mathbf{F}(\mathbf{x})$ was the vector of VCDs of the targeted tracer simulated by the forward model \mathbf{F} . S_a was the *a priori* emission error covariance matrix, which we assumed to be diagonal

The observation error covariance matrix in Eq. (1), S_o , was difficult to quantify, as it included contributions not only from the satellite retrieval, but also from the model representation of chemistry and transport. Zhu et al. (2016) and Chan Miller et al. (2017) compared vertical profiles of GEOS-Chem-simulated formaldehyde and glyoxal over the Southeast U.S. in summer against aircraft measurements. They reported that the simulated formaldehyde mixing ratios showed only a small bias ($-3\% \pm 2\%$) in the lower troposphere but were lower than the observations by 41% in the free troposphere, likely due to insufficient deep convection in the model (Zhu et al., 2016). The simulated glyoxal mixing ratios were within 20% of the observations in the mixed layer, but they were too low in the upper troposphere by more than a factor of two, also likely due to insufficient model vertical transport (Chan Miller et al., 2017). It should be noted that these errors assessed by Zhu et al. (2016) and Chan Miller et al. (2017) likely also included the errors associated with precursor emissions. Nevertheless, based on these assessments, we estimated that the model errors for formaldehyde and glyoxal VCDs to be $\pm 80\%$, $\pm 100\%$, respectively. Adding these estimated model errors in quadrature to the satellite retrieval errors (Section 2.3), we estimated that the observation error (S_o) of formaldehyde and glyoxal to be about $\pm 90\%$ and $\pm 150\%$, respectively.

The optimization of Eq. (1) was dependent on the relative weighting of the penalty error (S_a) and the prediction error (S_o), which were often incompletely represented. In addition, we found that due to the mathematical formulation of Eq. (1), the cost function $J(\mathbf{x})$ was heavily weighted by grids where the *a priori* estimates were too high, such that the optimization was less effective at increasing emissions

where the *a priori* emissions were too low. These issues were empirically addressed in inversion studies by the introduction of a regularization factor, γ , to adjust the relative weight of the penalty error. Henze et al. (2009) used the L-curve method (Hansen, 1998) to find an optimal γ value, which minimized the total cost function while balancing the prediction term and the penalty term. We followed that methodology and found a γ value of 0.01 for July, which we applied to all warmer months (March to October). An optimized γ value of 0.1 was found for January and applied to colder months.

Table 1 lists our inversion experiments. Figure S3 illustrates our protocol for the inversion experiments. We experimented with four different sets of satellite retrievals as constraints, with the goal of bracketing the possible range of top-down estimates for Chinese NMVOC emissions. The first two experiments (IE-1 and IE-2) constrained emissions using the formaldehyde and glyoxal VCDs observations from GOME-2A and OMI, respectively. Several studies showed that GOME-2A formaldehyde VCDs may be low by a factor of 1.3 to 1.7 (Lee et al., 2015; Zhu et al., 2016; Wang et al., 2017). As an “upper bound” constraint, we conducted a third inversion experiment (IE-3) constrained by 1.7 times the GOME-2A formaldehyde VCDs. We conducted a fourth inversion experiment (IE-4) constrained by OMI glyoxal VCDs alone to explore the impacts of glyoxal observations on the inversions.

3 Comparison of simulations using the *a priori* emissions against satellite observations and ground-based measurements

We first compared the formaldehyde and glyoxal VCDs simulated by the model (sampled at satellite overpass times) using the *a priori* emissions against those observed by GOME-2A and OMI, as well as against measurements at ground-based sites (Table S3). Figures 3 and 4 show the monthly mean formaldehyde VCDs observed by GOME-2A over China in 2007. Observed formaldehyde VCDs over China showed a distinct west-to-east gradient year-round, driven by the higher vegetation and population densities in eastern China. Observed formaldehyde VCDs were higher in summer than in winter, due to a combination of stronger biogenic emissions and photochemistry during the warmer months. In spring, GOME-2A formaldehyde VCDs were high over Southwest China and Southeast

Asia, reflecting the seasonal biomass burning emissions there. Highest formaldehyde VCDs were observed over the NCP in June, likely because of the large emissions from in-field crop residue burning.

Figures 3 and 4 compare the simulated monthly mean formaldehyde VCDs using the *a priori* emission against the GOME-2A formaldehyde VCDs. Table S4 summarizes the statistics of the comparison over eastern China. The *a priori* simulated formaldehyde VCDs generally reproduced the observed seasonal contrast and spatial patterns over eastern China, with correlation coefficients (R) between 0.74 and 0.94 year-round, except in December (R = 0.51). The *a priori* simulated formaldehyde VCDs were significantly higher than the GOME-2A observations over eastern China between late fall and winter (November, December, January, and February), with normalized mean biases (NMB) of 13% to 67%, implying an overestimate of the anthropogenic formaldehyde precursors in the *a priori* emission estimates. The *a priori* simulated formaldehyde VCDs were lower than the GOME-2A observations over eastern China during May to July (NMB between -11% to -6.4%), implying an underestimation of the emissions of formaldehyde precursors in the *a priori* during May to July.

A few ground-based measurements of tropospheric formaldehyde VCDs have been made in China using the Multi-Axis Differential Optical Absorption Spectrometry (MAX-DOAS) technique (Li et al., 2013; Vlemmix et al., 2015; Wang et al., 2017); these measurements (sampled at GOME-2A overpass time) are shown in Figure 3, Figure 4, and Table S3. In principle, these ground-based measurements are not directly comparable to the satellite-observed and model-simulated formaldehyde VCDs, due to the coarse spatial resolution of our analyses. Nevertheless, these ground-based measurements showed that (1) formaldehyde VCDs were higher during the warmer months relative to the colder months; (2) formaldehyde VCDs over Wuxi (in central eastern China) were higher than those over Xianghe (in northern China) and Back Garden (in southern China) for most months; (3) with the exception of June, when the formaldehyde VCDs over Xianghe were the highest among the three MAX-DOAS sites, reflecting the strong emissions from biomass burning in the NCP. Thus, the seasonal patterns shown in these few ground-based measurements were consistent with both the GOME-2A-observed and model-simulated formaldehyde VCDs.

Figure S4 compares the GOME-2A-observed and model-simulated formaldehyde VCDs against the monthly MAX-DOAS measurements at Xianghe (Vlemmix et al., 2015). The GOME-2A formaldehyde VCDs were consistent with the MAX-DOAS measurements in terms of the seasonal variation ($R = 0.9$) but showed an annual mean bias of -2.74×10^{15} molecules cm^{-2} . In comparison, by multiplying the GOME-2A formaldehyde VCD observations by 1.7, the annual mean bias against the MAX-DOAS measurements at Xianghe was reduced to 0.83×10^{15} molecules cm^{-2} . Figures 3 and 4 show that the bias between the satellite and MAX-DOAS measurements was also reduced at Wuxi when the GOME-2A formaldehyde VCDs were scaled up by 1.7. These findings offered some support for using the GOME-2A formaldehyde VCDs scaled by 1.7 as an upper-bound constraint for Chinese NMVOC emissions.

Figures 5 and 6 compare the monthly mean glyoxal VCDs observed by GOME-2A with those simulated by the model using *a priori* emission estimates. Similar to the case of formaldehyde, GOME-2A-observed glyoxal VCDs over China were higher in the east than in the west and higher in summer than in winter. High glyoxal VCDs were observed over the NCP in June and over Southwest China in spring, reflecting the strong seasonal biomass burning emissions. During winter (particularly in January), the GOME-2A glyoxal VCDs show an enhancement over eastern China, which was not apparent in the GOME-2A formaldehyde VCDs. This indicated that the glyoxal VCDs were more reflective of anthropogenic source than formaldehyde VCDs. The *a priori* simulated glyoxal VCDs were generally lower than the GOME-2A glyoxal VCDs over eastern China year-round, especially during the warmer months (NMB between -52% and -59% during May to September, Table S6). The only exception was over the NCP in winter, when the *a priori* simulated glyoxal VCDs were significantly higher than the GOME-2A observations. This suggested an overestimation of NMVOC sources over the NCP in winter and a substantial underestimation of NMVOCs sources over eastern China in summer, consistent with the constraints implied by the GOME-2A formaldehyde observations. During the transition months of April and October, when the anthropogenic and biogenic contributions to carbonyl productions were presumably more comparable, the simulated glyoxal VCDs were lower than the GOME-2A observations, while the simulated formaldehyde VCDs were higher than the GOME-2A observations (Figures 3 and 4). This likely indicated that the *a priori* inventory underestimated the emissions of NMVOC species that preferentially produced glyoxal (e.g. aromatics,

ethyne, ethene, and glyoxal), while overestimating the emissions of species that preferentially produced formaldehyde (e.g. $\geq C_4$ alkanes, $\geq C_3$ alkenes, and formaldehyde) during the transition months. Ground-based MAX-DOAS glyoxal measurements at Back Garden (a rural site in southern China) in July 2006 averaged $6.8(\pm 5.2) \times 10^{14}$ molecules cm^{-2} (Li et al., 2013), higher than both the GOME-2A-observed and simulated glyoxal VCDs. No other ground-based measurements were available to provide spatial and seasonal information.

Figures 7 and 8 compare the formaldehyde VCDs observed by OMI with those simulated by the model using *a priori* emission estimates. The spatial patterns and seasonal variations of the formaldehyde VCDs observed by OMI were similar to those observed by GOME-2A, with high formaldehyde over eastern China and during the warmer months. However, the OMI observations were approximately 30% lower than the GOME-2A observations over eastern China year-round. This difference may be due in part to the different satellite overpass times, or it may be due to the inherent biases between the GOME-2A and OMI formaldehyde VCD retrievals (De Smedt et al., 2012; González Abad et al., 2015). The *a priori* simulated formaldehyde VCDs (at OMI overpass time) were higher than the OMI observations over eastern China year-round (NMB between 22% and 70%, Table S7), suggesting an overestimation of NMVOC emissions year-round. The simulated formaldehyde VCDs at the OMI overpass time were also lower than those at GOME-2A overpass time by approximately 20% in all seasons, due to stronger photolysis of formaldehyde in the afternoon in the model. However, the MAX-DOAS measurements at three Chinese sites all showed higher formaldehyde VCDs at the OMI overpass time than at the GOME-2A overpass time (Li et al., 2013; Vlemmix et al., 2015; Wang et al., 2017).

Figures 9 and 10 show the monthly mean glyoxal VCDs observed by OMI and those simulated by the model. Valid OMI glyoxal observations were relatively sparse over China, especially during the cold seasons. The seasonal and spatial patterns of the glyoxal VCDs observed by OMI were generally consistent with those observed by GOME-2A over eastern China. However, the glyoxal VCDs observed by OMI were consistently higher than those observed by GOME-2A, except in January. MAX-DOAS measurements of glyoxal at Back Garden in July 2006 were also higher in the afternoon

than in mid-morning (Li et al., 2013). In contrast, the *a priori* simulated glyoxal VCDs at OMI overpass time were lower than those at GOME-2A overpass time. This discrepancy among the glyoxal diurnal cycles represented by the MAX-DOAS measurements and the model indicated an uncertainty in the simulated local glyoxal budget. The *a priori* simulated glyoxal VCDs were lower than the OMI observations throughout the year (NMB between -32% to -66%, Table S8) and especially from March to October, indicating an underestimation of NMVOC sources in the *a priori* year-round.

It thus appeared that the constraints on Chinese NMVOC emissions indicated by the OMI formaldehyde and glyoxal observations were contradictory. There are two possible causes for this apparent contradiction. Firstly, the simulated photochemical budgets of formaldehyde and glyoxal during the local afternoon may be in error, which would also explain why the MAX-DOAS measurements of formaldehyde and glyoxal VCDs were both higher in the afternoon than in the morning, while the model showed an opposite diurnal contrast. Secondly, it is also possible that there were different inherent biases in the OMI formaldehyde and glyoxal retrievals.

4 Inversion experiments of Chinese NMVOC emissions

4.1 *A posteriori* formaldehyde and glyoxal VCDs from inversion experiments

The qualitative analyses in Section 3 showed that the GOME-2A and OMI retrievals of formaldehyde and glyoxal VCDs provided disparate information on seasonal Chinese NMVOC emissions. Therefore, our four inversion experiments using different satellite observations as constraints represented the range of probable top-down estimates given current satellite observations. Here we first examined how the inversion experiments optimized the *a posteriori* formaldehyde and glyoxal VCDs and the resulting effects on the top-down monthly Chinese NMVOC emission estimates. Figure S7 shows the changes in the normalized cost functions over China in the four inversion experiments. Relative to their respective initial cost function values, the optimized cost function values were reduced by 8% to 75% for all four experiments. Figure 2 shows the top-down monthly Chinese NMVOC emission estimates from the four inversion experiments and compares them against the *a priori* emission estimates. Figure S6 compares the *a priori* and *a posteriori* emission estimates for anthropogenic glyoxal precursors.

Figures 3 to 6 show the *a posteriori* simulated monthly mean formaldehyde and glyoxal VCDs from the GOME-2A formaldehyde and glyoxal inversion experiment (IE-1). Overall, IE-1 greatly improved the agreement between the *a posteriori* VCDs and the GOME-2A observations for both formaldehyde (Table S4) and glyoxal (Table S6) over eastern China for most months. The optimization was especially effective in optimizing the spatial pattern of the *a posteriori* formaldehyde VCDs, such that the *a posteriori* R against the GOME-2A formaldehyde VCDs exceeded 0.85 over eastern China for all twelve months (Table S4). Relative to the *a priori* VCDs, the *a posteriori* VCDs of formaldehyde and glyoxal both decreased over NCP in winter and increased over eastern China between May and September. During the transition months of April and October, the *a posteriori* formaldehyde VCDs decreased relative the *a priori*, while the *a posteriori* glyoxal VCDs increased relative to the *a priori*. Figures 2 and Figure S6 illustrated how these changes in *a posteriori* formaldehyde and glyoxal VCDs affected the top-down monthly NMVOC emission estimates. For IE-1, the estimated emissions of all NMVOC species were reduced in winter but enhanced between May and September. In April and October, however, IE-1 decreased the total NMVOC emissions while preferentially increasing the emissions of anthropogenic glyoxal precursors.

Figures 7 to 10 show the *a posteriori* monthly mean formaldehyde and glyoxal VCDs from the OMI formaldehyde/glyoxal inversion experiment (IE-2). IE-2 was effective in reducing the *a posteriori* formaldehyde VCDs over eastern China year-round to better agree with the OMI formaldehyde observations (Table S7). However, IE-2 increased the *a posteriori* glyoxal VCDs only slightly and was less effective in bringing agreement with the OMI glyoxal observations (Table S8). Figure 2 shows that the *a posteriori* NMVOC emission estimates from IE-2 were lower than the *a priori* estimates for all months. This was due to a combination of factors at work in the inversion. The low formaldehyde observations from OMI in all months drove a large reduction in the emissions of NMVOCs that produced only formaldehyde ($\geq C_4$ alkanes and $\geq C_3$ alkenes from anthropogenic activities, as well as primary formaldehyde from biomass burning). At the same time, the relatively high glyoxal observations from OMI drove an increase in the emissions of NMVOCs that produced mainly glyoxal (ethene, ethyne, and aromatics from anthropogenic activities, as well as primary glyoxal from biomass burning). For precursors that produced large amounts of both formaldehyde and glyoxal (most importantly biogenic isoprene), the inversion reduced the top-down emissions as the formaldehyde

observations had more weight in the cost function than the glyoxal observations, due to the lower observational errors in the formaldehyde VCDs. These findings showed the importance of well-characterized retrievals with reliable error estimates in inversion studies.

Figures 3 and 4 showed the *a posteriori* formaldehyde VCDs from the inversion experiment IE-3, which was constrained by the GOME-2A-observed formaldehyde VCDs scaled by a factor of 1.7. The *a posteriori* formaldehyde VCDs in IE-3 increased further over eastern China during the warmer months relative to IE-1, especially over the NCP and central China in summer. In December and January, the scaled-up GOME-2A observations over eastern China were still lower than the simulated formaldehyde VCDs using the *a priori* emissions, leading to a reduction in the *a posteriori* formaldehyde VCDs over East China (Table S5). Figure 2 shows that the top-down monthly emission estimates for all NMVOC species were lower than the *a priori* in November, December, January, and February, and higher than the *a priori* for the warmer months. Consequently, although no observations of glyoxal were used as constraints in IE-3, the *a posteriori* glyoxal VCDs also decreased in winter and increased in summer, which were in better agreement with the GOME-2A observations (Figures 5 and 6). This is consistent with our analyses in Section 3: the constraints exerted by the GOME-2A formaldehyde and glyoxal observations were consistent in winter and in summer, when the NMVOC emissions were dominated by anthropogenic and biogenic sources, respectively. However, IE-3 had almost no effects on the *a posteriori* glyoxal VCDs and the top-down emission estimates of anthropogenic glyoxal precursors in April and October. This demonstrated the necessity of glyoxal observations on constraining the emissions of NMVOC species that preferentially produced glyoxal, including most importantly the aromatics.

The impacts of satellite glyoxal observations on constraining Chinese glyoxal precursors emission estimates was further demonstrated in IE-4. Figures 9 and 10 show that the *a posteriori* glyoxal VCDs from IE-4 were in better agreement with the OMI glyoxal observations for all months (Table S8). Figure 2 and Figure S6 show that this increase in the *a posteriori* glyoxal VCDs in IE-4 was achieved by substantially increasing the emission estimates of anthropogenic glyoxal precursors for all months. In summer, the emissions of biogenic isoprene (precursor to both glyoxal and formaldehyde) also increased. As a result, the *a posteriori* formaldehyde VCDs in IE-4 increased in summer but remained

similar to the *a priori* simulation for the other months (Figures 7 and 8, Table S7).

4.2 Top-down estimates of Chinese NMVOC emissions from inversion experiments

Table 1 and Figure 11 show the top-down estimates for Chinese annual NMVOC emissions from the four inversion experiments and compare them against the *a priori*. Our top-down annual total estimates for Chinese NMVOCs ranged from 30.7 to 49.5 Tg y⁻¹, compared to the 38.3 Tg y⁻¹ of the *a priori*. The highest top-down estimate was from IE-3, constrained by 1.7 times the GOME-2A formaldehyde VCD observations. The lowest top-down estimate was from IE-2, mainly driven by the relatively low formaldehyde observations from OMI.

Anthropogenic sources constituted 44%-53% of the top-down total NMVOC emissions. The lowest top-down total anthropogenic emission estimate was from IE-2 (16.4 Tg y⁻¹). All four inversion experiments consistently showed larger annual emissions of anthropogenic glyoxal precursors than the *a priori* (Figure 11). In particular, our top-down estimates for anthropogenic aromatics ranged from 5.5 to 7.9 Tg y⁻¹, consistently larger than the *a priori* of 5.4 Tg y⁻¹ (Li et al., 2017). The highest top-down anthropogenic glyoxal precursors (including aromatics, ethyne, ethane, and glyoxal) emissions estimate was from IE-4 (12.3 Tg y⁻¹), which reflected the strong impacts of the OMI glyoxal observations on constraining anthropogenic NMVOC emissions.

The top-down estimates for biogenic NMVOCs emissions from IE-1, IE-3, and IE-4 ranged between 20.0 and 22.8 Tg y⁻¹ (top-down biogenic isoprene emission estimates between 9.8 and 11.7 Tg y⁻¹), which were significantly larger than the *a priori*. As a result, the contrast between the NMVOC emissions in summer and those in winter were greatly enhanced in the top-down estimates in these three inversion experiments, relative to the *a priori* (Figure 2). The exception was IE-2, which estimated the biogenic NMVOC emissions to be 12.2 Tg y⁻¹ (including 5.4 Tg y⁻¹ of isoprene). The top-down estimate for biomass burning NMVOC emissions from the four inversion experiments were between 2.08 to 3.13 Tg y⁻¹, with the largest top-down estimate driven by the scaled-up GOME-2A formaldehyde VCDs (IE-3).

Figure 12 shows the spatial distribution of the scale factors for the Chinese annual NMVOC emissions from each of the four inversion experiments relative to the *a priori* emission estimates. The use of GOME-2A formaldehyde and glyoxal observations as constraints in IE-1 led to a domain-wide increase in biogenic NMVOC emissions, except in the northeast. IE-1 also found an increase in biomass burning emissions over the NCP in June. In contrast, anthropogenic NMVOC emissions were slightly reduced over northeast, north, and southwest China. In IE-3, the annual NMVOC emissions over eastern China increased for all three sources, due to constraints exerted by the scaled-up GOME-2A formaldehyde VCDs. The optimized emission scale factors from IE-2 and IE-4 were of opposite signs. Using only OMI glyoxal observations as constraints in IE-4 led to a domain-wide increase in NMVOC emissions from all sectors. However, when constraints of the relatively low OMI formaldehyde observations were added in IE-2, the top-down NMVOC emission estimates decreased across the domain.

As discussed previously, our four inversion experiments using different satellite retrievals as constraints represented the range of probable top-down estimates given currently-available satellite observations. To represent the difference between these top-down estimates relative to the *a priori*, we averaged the top-down estimates from the four inversion experiments. Our averaged top-down estimate for Chinese total annual NMVOC emissions was 41.9 Tg y⁻¹, including 20.2 Tg y⁻¹, 19.2 Tg y⁻¹, and 2.48 Tg y⁻¹ from anthropogenic, biogenic, and biomass burning sources, respectively. Our average emission estimate for anthropogenic aromatics was 6.5 Tg y⁻¹, which was 20% larger than the *a priori* estimate of Li et al. (2017).

Figure 1 shows the spatial distributions of our averaged top-down Chinese NMVOC emissions and the scale factors relative to the *a priori*. Our averaged top-down estimate for Chinese NMVOC emissions were spatially consistent with the *a priori*, but the total fluxes were larger than the *a priori* throughout eastern China by 10% to 30%. In particular, we found a 40% increase in the biomass burning emissions over the NCP. We also found a 10%-30% increase in the anthropogenic NMVOC emissions in coastal eastern China. Large increases in the biogenic emissions were found near the northwestern border of China and along the northeast-to-southwest division line of vegetation density. This potentially indicated an underestimation of biogenic NMVOC emission from semi-arid ecosystems in the MEGAN inventory.

683

684 **5 Comparison with previous estimates of Chinese NMVOC emissions**

685 Table 2 compares our top-down estimates of Chinese NMVOC emissions for the year 2007 against
686 estimates in the literature for the years between 2000 and 2014. It should be noted that most bottom-up
687 anthropogenic and biomass burning emission inventories quantified total NMVOC emissions using
688 emission factors for total NMVOCs. As a result, bottom-up estimates for anthropogenic and biomass
689 burning sources often included additional NMVOC species not represented here in our study.

690

691 Our top-down estimate for biogenic NMVOC emissions range from 12.2 to 22.8 Tg y⁻¹, on average 11%
692 larger than the *a priori* estimate calculated by the MEGAN algorithm (Guenther et al., 2006). Our
693 top-down estimate for isoprene emission ranged from 5.4 to 11.7 Tg y⁻¹, bracketing the previous
694 bottom-up estimates of 7.5 to 9.9 Tg y⁻¹ (Guenther et al., 2006; Stavrakou et al., 2014; Sindelarova et
695 al., 2014). Stavrakou et al. (2015) used GOME-2A and OMI formaldehyde VCDs in 2010 to derive
696 top-down estimates of isoprene emissions over China of 5.9 Tg y⁻¹ (using GOME-2A observations as
697 constraints) and 6.5 Tg y⁻¹ (using OMI observations as constraints), respectively. In comparison, our
698 top-down isoprene emission estimates constrained by GOME-2A and OMI observations of both
699 formaldehyde and glyoxal were 9.8 Tg y⁻¹ (from IE-1) and 5.4 Tg y⁻¹ (from IE-2), respectively. Our
700 top-down estimates constrained by GOME-2A observations was larger than that of Stavrakou et al.
701 (2015) due to the additional glyoxal constraints. Our isoprene emission constrained by OMI
702 observations was lower than that of Stavrakou et al. (2015). This was because the OMI formaldehyde
703 VCDs over China we used were systematically lower than the OMI formaldehyde VCDs used in
704 Stavrakou et al. (2015), which was retrieved by De Smedt et al. (2015). A later study by Stavrakou et al.
705 (2017) using OMI formaldehyde VCDs estimated the average Chinese biogenic isoprene emissions for
706 the years 2005 to 2014 to be 5.8 Tg y⁻¹, consistent with our top-down estimate from IE-2.

707

708 Our top-down estimates for Chinese annual biomass burning NMVOC emissions ranged from 2.08 to
709 3.13 Tg y⁻¹, in good agreement with the bottom-up estimates of Huang et al. (2012) and the top-down
710 estimates of Stavrakou et al. (2015) (Table 2). Similar to the findings in Fu et al. (2007) and Stavrakou
711 et al. (2015, 2016), our study also highlighted the large emissions from crop residue over the NCP in

June, which were severely underestimated in some previous studies. Bo et al. (2008) and Wu et al. (2016) estimated the Chinese biomass burning NMVOC emissions to be 3.32 to 4.2 Tg y⁻¹, but only 25% to 30% of these emissions were from open burning of crop residues; the rest were emitted from biofuel burning, which we categorized as anthropogenic in this study. The GFED3 inventory (van der Werf et al., 2010), based on satellite burned area observations, severely underestimated biomass burning emissions over China, particularly those associated with crop residue burning. The updated GFED4 (van der Werf et al., 2017) partially accounted for emissions for small fires, but its estimate for Chinese biomass burning NMVOC emissions was still lower than our top-down estimates by at least a factor of two.

Previous bottom-up estimates of Chinese anthropogenic NMVOC emissions ranged widely from 12.7 to 35.46 Tg y⁻¹ (Bo et al., 2008; Zhang et al., 2009; Cao et al., 2011; Kurokawa et al., 2013; Li et al., 2017; Wu et al., 2016; Granier et al., 2017; Huang et al., 2017) due to the use of different emission factors, activity data, and statistical models. Previous top-down estimates of Chinese anthropogenic NMVOC emissions for the years 2007 to 2014 ranged from 20.6-34.2 Tg y⁻¹ (Liu et al., 2012; Stavrou et al., 2015, 2017). Our top-down estimates had a smaller range between 16.4 to 23.6 Tg y⁻¹. Our top-down estimates for anthropogenic aromatics (5.5 to 7.9 Tg y⁻¹) were approximately middle-of-the-range relative to previous estimates of 2.4-13.4 Tg y⁻¹. The large difference between previous top-down estimates and our top-down estimates of anthropogenic NMVOCs were predominantly due to the choices of satellite observation constraints, and to a lesser extent due to the choices of chemical transport model, the NMVOC species modeled, and the *a priori* emission estimates. Specifically, the much higher estimate of anthropogenic aromatic emission by Liu et al. (2012) (13.4 Tg y⁻¹) compared to our top-down estimates (5.5-7.9 Tg y⁻¹) was due to (1) the higher glyoxal VCDs observed by the SCIAMACHY instrument compared to those observed by GOME-2A and OMI over China; (2) the assumption made by Liu et al. (2012) that all anomalous glyoxal was produced by aromatics; and (3) the lower yields of glyoxal from aromatics oxidation used in Liu et al. (2012) than those used in our model.

6 Impacts on simulated surface ozone and secondary organic aerosol levels over China

As discussed above, three out of our four inversion experiments showed a stronger seasonal contrast in the top-down NMVOC emission estimates between summer and winter (Figure 2). We evaluated the impacts of this stronger seasonal contrast in NMVOC emissions on surface ozone and secondary organic carbon (SOC) aerosol concentrations by driving the GEOS-Chem model with the *a priori* NMVOC emission estimates and with the average top-down emission estimates from our four inversion experiments, respectively (Table 1).

Figure 13 compares the monthly mean afternoon (13 to 17 local time) surface ozone concentrations simulated using our averaged top-down emission estimates against those simulated using the *a priori* emissions for June and December 2007. Also shown are surface observations at representative regional sites (Li et al., 2007; Xu et al., 2008; J. M. Zhang et al., 2009; Zheng et al., 2010; Wang et al., 2012; Wang et al., 2015; Li and Bian, 2015; Sun et al., 2016; Xu et al., 2016) (Table S9). Using the *a priori* emissions, the highest simulated afternoon surface ozone concentrations were between 90-100 ppb over the NCP in June. This was lower than the observations at two sites in the NCP, including at a rural site outside Beijing (100 to 120 ppb) and at Mt. Tai (108 ppb). In comparison, by using our averaged top-down NMVOC emission estimate, the simulated afternoon surface ozone increased by 1 to 8 ppb over eastern China in June and were in better agreement with the observations (reducing the bias from -3.4 ppb to -0.7 ppb, Table S9). In December, the simulated afternoon surface ozone using the *a priori* emissions consistently overestimated the observed concentrations in eastern China. In comparison, by using our averaged top-down NMVOC emission estimates, the simulated afternoon surface ozone over eastern China decreased by 1 to 10 ppb, again in better agreement with the observations (mean bias reduced from 12 ppb to 6.9 ppb, Table S9). It thus appeared that our average top-down NMVOC emission estimates, with stronger seasonal contrast in NMVOC emissions compared to the *a priori*, improved the simulation of regional ozone when compared to surface measurements.

Figure S8 compares the simulated monthly mean surface SOC concentrations using our averaged top-down NMVOCs emissions against those simulated using the *a priori* NMVOC emissions for January and June in 2007. Also shown are the SOC measurements at 12 surface sites in June of 2006

and 2007 from Zhang et al. (2012) (Table S10). By driving the model with our average top-down NMVOC emissions, the simulated surface SOC concentrations in June increased by 0.1 to 0.8 $\mu\text{gC m}^{-3}$ over eastern China relative to the simulation using the *a priori* NMVOC emissions. This increase in simulated SOC concentrations brought the model to be closer to the surface measurements, but the model still severely underestimated observed SOC concentrations. We note that our version of the GEOS-Chem model only included two pathways for secondary organic aerosol formation: (1) the reversible partitioning of semi-volatile products from the oxidation of isoprene, monoterpenes, and aromatics formation pathways (Liao et al., 2007; Henze et al., 2008), and (2) the irreversible uptake of dicarbonyl by aqueous aerosols and cloud drops (Fu et al., 2008). Other pathways, such as the atmospheric aging of semi-volatile and intermediate volatility organic compounds (S/IVOC), have been shown to be an important source of secondary organic aerosol (Robinson et al., 2007; Pye and Seinfeld, 2010) but they were not included in our version of GEOS-Chem. Regardless, the precursors and formation pathways of secondary organic aerosols in China are still poorly understood (Fu et al., 2012), such that no quantitative conclusions can be drawn regarding the impacts of our top-down NMVOC emission estimates on regional secondary organic aerosol formation.

7 Conclusions

We used the GEOS-Chem model and its adjoint, as well as satellite observations of tropospheric column concentrations of formaldehyde and glyoxal, to constrain monthly Chinese NMVOC emissions from anthropogenic, biogenic, and biomass burning sources for the year 2007. We updated the gas-phase chemistry in the GEOS-Chem model and constructed its adjoint. The *a priori* NMVOC emission estimates from biogenic, anthropogenic, and biomass burning sources were taken from the inventories developed by Guenther et al. (2006), Li et al (2014, 2017), and Huang et al. (2012), as well as van der Werf et al. (2010), respectively. We conducted four inversion experiments, which were constrained by the formaldehyde and glyoxal observations from GOME-2A (IE-1), the formaldehyde and glyoxal observations from OMI (IE-2), the formaldehyde observations from GOME-2A scaled by 1.7 (IE-3), and the glyoxal observations from OMI (IE-4), respectively. The results from these experiments represented the range of probable top-down NMVOC emission estimates for China given current satellite observation constraints.

Our top-down estimates of total annual Chinese NMVOC emission from the four inversion experiments ranged from 30.7 to 49.5 Tg y⁻¹. Our top-down estimates of Chinese anthropogenic NMVOC emission was 16.4 to 23.6 Tg y⁻¹. In particular, our top-down estimates for Chinese anthropogenic aromatic emissions ranged from 5.5 to 7.9 Tg y⁻¹, much smaller than the top-down estimate of 13.4 Tg y⁻¹ by Liu et al. (2012). Our top-down estimate of Chinese biogenic NMVOC emission ranged from 12.2 to 22.8 Tg y⁻¹, with 5.4 to 11.7 Tg y⁻¹ attributed to isoprene. Our top-down estimate for Chinese biomass burning NMVOC emission range from 2.08 to 3.13 Tg y⁻¹ and was mostly associated with seasonal open burning of crop residue after local harvests, such as those over the NCP in June.

809

Three out of our four inversion experiments showed a stronger seasonal contrast in the top-down NMVOC emission estimates between summer and winter, relative to the *a priori* emission estimates. By applying this stronger seasonal contrast in monthly NMVOC emissions in the model, the simulated afternoon surface ozone concentrations over eastern China increased by 1 to 8 ppb in June and decreased by 1 to 10 ppb in December relative to the simulation using the *a priori* emissions, and the model was brought to better agreement with regional surface ozone measurements. Similarly, compared to the *a priori* simulation, the simulated monthly mean SOC concentrations driven by our top-down NMVOCs emissions increased by 0.1 to 0.8 µgC m⁻³ over Eastern China in June. This increase in simulated SOC concentrations reduced, but did not eliminate, the large low biases in the simulated SOC concentrations relative to the surface measurements in June.

820

We concluded that formaldehyde and glyoxal observations from GOME-2A and OMI provide quantitative constraints on the monthly emissions of Chinese NMVOCs. In particular, the simultaneous use of the observations of both species helped distinguish NMVOC precursors and thus provided better quantification of individual sources. However, better validation of these satellite data over China are urgently needed, particularly to resolve the apparent discrepancies between different retrievals for the same species. The monthly inversions presented in this work, conducted at 5° longitude × 4° latitude resolution due to limited computation resources, quantified the Chinese NMVOC emissions on regional/sub-regional scales. Future inversions and sensitivity studies targeting shorter periods of time

may be conducted on finer resolutions to quantify Chinese NMVOC emissions and to evaluate their impacts on photochemistry at city cluster scales.

Acknowledgements

This work was supported by the Ministry of Science and Technology of China (2014CB441303) and the National Natural Sciences Foundation of China (41461164007, 41222035). We thank the National Super Computer Center in Tianjin for providing computational support and the QA4ECV campaign for providing the MAX-DOAS measurements at Xianghe. DKH was supported by the National Strategic Project-Fine particle of the National Research Foundation of Korea (NRF) funded by the Ministry of Science and ICT (MSIT), the Ministry of Environment (ME), and the Ministry of Health and Welfare (MOHW) (2017M3D8A1092052).

References

- Akagi, S. K., Yokelson, R. J., Wiedinmyer, C., Alvarado, M. J., Reid, J. S., Karl, T., Crounse, J. D., and Wennberg, P. O.: Emission factors for open and domestic biomass burning for use in atmospheric models, *Atmos. Chem. Phys.*, 11, 4039-4072, doi: 10.5194/acp-11-4039-2011, 2011.
- Arey, J., Obermeyer, G., Aschmann, S. M., Chattopadhyay, S., Cusick, R. D., and Atkinson, R.: Dicarbonyl Products of the OH Radical-Initiated Reaction of a Series of Aromatic Hydrocarbons, *Environ. Sci. Technol.*, 43, 683-689, doi: 10.1021/es8019098, 2009.
- Barkley, M. P., Palmer, P. I., Kuhn, U., Kesselmeier, J., Chance, K., Kurosu, T. P., Martin, R. V., Helmig, D., and Guenther, A.: Net ecosystem fluxes of isoprene over tropical South America inferred from Global Ozone Monitoring Experiment (GOME) observations of HCHO columns, *J. Geophys. Res.*, 113, doi: 10.1029/2008jd009863, 2008.
- Barkley, M. P., Palmer, P. I., De Smedt, I., Karl, T., Guenther, A., and Van Roozendaal, M.: Regulated large-scale annual shutdown of Amazonian isoprene emissions?, *Geophys. Res. Lett.*, 36, doi:10.1029/2008gl036843, 2009.
- Barkley, M. P., Smedt, I. D., Van Roozendaal, M., Kurosu, T. P., Chance, K., Arneth, A., Hagberg, D., Guenther, A., Paulot, F., Marais, E., and Mao, J.: Top-down isoprene emissions over tropical South America inferred from SCIAMACHY and OMI formaldehyde columns, *J. Geophys. Res. Atmos.*, 118,

860 6849-6868, doi:10.1002/jgrd.50552, 2013.

861 Bey, I., Jacob, D. J., Yantosca, R. M., Logan, J. A., Field, B. D., Fiore, A. M., Li, Q., Liu, H. Y.,
862 Mickley, L. J., and Schultz, M. G.: Global modeling of tropospheric chemistry with assimilated
863 meteorology: Model description and evaluation, *J. Geophys. Res.*, 106, 23073-23095, doi:
864 10.1029/2001JD000807, 2001.

865 Bloss, C., Wagner, V., Jenkin, M. E., and Volkamer, R.: Development of a detailed chemical
866 mechanism (MCMv3.1) for the atmospheric oxidation of aromatic hydrocarbons, *Atmos. Chem. Phys.*,
867 5, 641-664, doi:10.5194/acp-5-641-2005, 2005.

868 Bo, Y., Cai, H., and Xie, S. D.: Spatial and temporal variation of historical anthropogenic NMVOCs
869 emission inventories in China, *Atmos. Chem. Phys.*, 8, 7297-7316, doi: 10.5194/acp-8-7297-2008,
870 2008.

871 Cao, G., Zhang, X., Gong, S., An, X., and Wang, Y.: Emission inventories of primary particles and
872 pollutant gases for China, *Chin. Sci. Bull.*, 56, 781-788, doi:10.1007/s11434-011-4373-7, 2011.

873 Chan Miller, C., Gonzalez Abad, G., Wang, H., Liu, X., Kurosu, T., Jacob, D. J., and Chance, K.:
874 Glyoxal retrieval from the Ozone Monitoring Instrument, *Atmos. Meas. Tech.*, 7, 3891-3907,
875 doi:10.5194/amt-7-3891-2014, 2014.

876 Chan Miller, C., Jacob, D. J., Abad, G. G., and Chance, K.: Hotspot of glyoxal over the Pearl River
877 delta seen from the OMI satellite instrument: implications for emissions of aromatic hydrocarbons,
878 *Atmos. Chem. Phys.*, 16, 4631-4639, doi: 10.5194/acp-16-4631-2016, 2016.

879 Chan Miller, C., Jacob, D. J., Marais, E. A., Yu, K. R., Travis, K. R., Kim, P. S., Fisher, J. A., Zhu, L.,
880 Wolfe, G. M., Hanisco, T. F., Keutsch, F. N., Kaiser, J., Min, K. E., Brown, S. S., Washenfelder, R. A.,
881 Abad, G. G., and Chance, K.: Glyoxal yield from isoprene oxidation and relation to formaldehyde:
882 chemical mechanism, constraints from SENEX aircraft observations, and interpretation of OMI
883 satellite data, *Atmos. Chem. Phys.*, 17, 8725-8738, doi: 10.5194/acp-17-8725-2017, 2017.

884 Chance, K.: Analysis of BrO measurements from the Global Ozone Monitoring Experiment, *Geophys.*
885 *Res. Lett.*, 25, 3335-3338, doi: 10.1029/98gl52359, 1998.

886 Curci, G., Palmer, P. I., Kurosu, T. P., Chance, K., and Visconti, G.: Estimating European volatile
887 organic compound emissions using satellite observations of formaldehyde from the Ozone Monitoring
888 Instrument, *Atmos. Chem. Phys.*, 10, 11501-11517, doi: 10.5194/acp-10-11501-2010, 2010.

889 Daescu, D. N., Sandu, A., and Carmichael, G. R.: Direct and adjoint sensitivity analysis of chemical
890 kinetic systems with KPP: II—numerical validation and applications, *Atmos. Environ.*, 37, 5097-5114,
891 doi:10.1016/j.atmosenv.2003.08.020, 2003.

892 De Smedt, I., Van Roozendaal, M., Stavrou, T., Müller, J. F., Lerot, C., Theys, N., Valks, P., Hao, N.,
893 and van der A, R.: Improved retrieval of global tropospheric formaldehyde columns from
894 GOME-2/MetOp-A addressing noise reduction and instrumental degradation issues, *Atmos. Meas.*
895 *Tech.*, 5, 2933-2949, doi:10.5194/amt-5-2933-2012, 2012.

896 De Smedt, I., Stavrakou, T., Hendrick, F., Danckaert, T., Vlemmix, T., Pinardi, G., Theys, N., Lerot, C.,
897 Gielen, C., Vigouroux, C., Hermans, C., Fayt, C., Veefkind, P., Müller, J. F., and Van Roozendael, M.:
898 Diurnal, seasonal and long-term variations of global formaldehyde columns inferred from combined
899 OMI and GOME-2 observations, *Atmos. Chem. Phys.*, 15, 12519-12545, doi:
900 10.5194/acp-15-12519-2015, 2015.

901 Dufour, G., Wittrock, F., Camredon, M., Beekmann, M., Richter, A., Aumont, B., and Burrows, J. P.:
902 SCIAMACHY formaldehyde observations: constraint for isoprene emission estimates over Europe?,
903 *Atmos. Chem. Phys.*, 9, 1647-1664, doi:10.5194/acp-9-1647-2009, 2009.

904 Fu, T. M., Cao, J. J., Zhang, X. Y., Lee, S. C., Zhang, Q., Han, Y. M., Qu, W. J., Han, Z., Zhang, R.,
905 Wang, Y. X., Chen, D., and Henze, D. K.: Carbonaceous aerosols in China: top-down constraints on
906 primary sources and estimation of secondary contribution, *Atmos. Chem. Phys.*, 12, 2725-2746, doi:
907 10.5194/acp-12-2725-2012, 2012.

908 Fu, T.-M., Jacob, D. J., Palmer, P. I., Chance, K., Wang, Y. X., Barletta, B., Blake, D. R., Stanton, J. C.,
909 and Pilling, M. J.: Space-based formaldehyde measurements as constraints on volatile organic
910 compound emissions in east and south Asia and implications for ozone, *J. Geophys. Res.*, 112, doi:
911 10.1029/2006jd007853, 2007.

912 Fu, T.-M., Jacob, D. J., Wittrock, F., Burrows, J. P., Vrekoussis, M., and Henze, D. K.: Global budgets
913 of atmospheric glyoxal and methylglyoxal, and implications for formation of secondary organic
914 aerosols, *J. Geophys. Res.*, 113, doi:10.1029/2007jd009505, 2008.

915 González Abad, G., Liu, X., Chance, K., Wang, H., Kurosu, T. P., and Suleiman, R.: Updated
916 Smithsonian Astrophysical Observatory Ozone Monitoring Instrument (SAO OMI) formaldehyde
917 retrieval, *Atmos. Meas. Tech.*, 8, 19-32, doi:10.5194/amt-8-19-2015, 2015.

918 Gonzi, S., Palmer, P. I., Barkley, M. P., De Smedt, I., and Van Roozendael, M.: Biomass burning
919 emission estimates inferred from satellite column measurements of HCHO: Sensitivity to co-emitted
920 aerosol and injection height, *Geophys. Res. Lett.*, 38, doi: 10.1029/2011gl047890, 2011.

921 Granier, C., Doumbia, T., Granier, L., Sindelarova, K., Frost, G., Bouarar, I., Lioussé, C., Darras, S.
922 and Stavrakou, J.: Anthropogenic emissions in Asia, *Air Pollution in Eastern Asia : an integrated*
923 *perspective*, eds. Bouarar, I., Wang, X., Brasseur, G., Springer international Publishing,
924 doi:10.1007/978-3-319-59489-7-6, pp. 107-133, 2017.

925 Guenther, A. B., Jiang, X., Heald, C. L., Sakulyanontvittaya, T., Duhl, T., Emmons, L. K., and Wang,
926 X.: The Model of Emissions of Gases and Aerosols from Nature version 2.1 (MEGAN2.1): an extended
927 and updated framework for modeling biogenic emissions, *Geosci. Model Dev.*, 5, 1471-1492, doi:
928 10.5194/gmd-5-1471-2012, 2012.

929 Guenther, A., Karl, T., Harley, P., Wiedinmyer, C., Palmer, P. I., and Geron, C.: Estimates of global
930 terrestrial isoprene emissions using MEGAN (Model of Emissions of Gases and Aerosols from Nature),
931 *Atmos. Chem. Phys.*, 6, 3181-3210, doi: 10.5194/acp-6-3181-2006, 2006.

932 Hallquist, M., Wenger, J. C., Baltensperger, U., Rudich, Y., Simpson, D., Claeys, M., Dommen, J.,

933 Donahue, N. M., George, C., Goldstein, A. H., Hamilton, J. F., Herrmann, H., Hoffmann, T., Iinuma, Y.,
 934 Jang, M., Jenkin, M. E., Jimenez, J. L., Kiendler-Scharr, A., Maenhaut, W., McFiggans, G., Mentel, T.
 935 F., Monod, A., Prevot, A. S. H., Seinfeld, J. H., Surratt, J. D., Szmigielski, R., and Wildt, J.: The
 936 formation, properties and impact of secondary organic aerosol: current and emerging issues,
 937 *Atmospheric Chemistry and Physics*, 9, 5155-5236, doi: 10.5194/acp-9-5155-2009, 2009.

938 Han, K. M., Park, R. S., Kim, H. K., Woo, J. H., Kim, J., and Song, C. H.: Uncertainty in biogenic
 939 isoprene emissions and its impacts on tropospheric chemistry in East Asia, *Sci. Total Environ.*, 463-464,
 940 754-771, doi: 10.1016/j.scitotenv.2013.06.003, 2013.

941 Hansen, P. C.: Rank-deficient and discrete ill-posed problems: numerical aspects of linear inversion,
 942 SIAM, Philadelphia, 1998.

943 Hays, M. D., Geron, C. D., Linna, K. J., Smith, N. D., and Schauer, J. J.: Speciation of gas-phase and
 944 fine particle emissions from burning of foliar fuels, *Environ. Sci. Technol.*, 36, 2281-2295,
 945 doi:10.1021/es0111683, 2002.

946 Henze, D. K., Hakami, A., and Seinfeld, J. H.: Development of the adjoint of GEOS-Chem, *Atmos.*
 947 *Chem. Phys.*, 7, 2413-2433, doi: 10.5194/acp-7-2413-2007, 2007.

948 Henze, D. K., Seinfeld, J. H., and Shindell, D. T.: Inverse modeling and mapping US air quality
 949 influences of inorganic PM_{2.5} precursor emissions using the adjoint of GEOS-Chem, *Atmos. Chem.*
 950 *Phys.*, 9, 5877-5903, doi:10.5194/acp-9-5877-2009, 2009.

951 Henze, D. K., Seinfeld, J. H., Ng, N. L., Kroll, J. H., Fu, T. M., Jacob, D. J., and Heald, C. L.: Global
 952 modeling of secondary organic aerosol formation from aromatic hydrocarbons: high- vs. low-yield
 953 pathways, *Atmos. Chem. Phys.*, 8, 2405-2420, doi:10.5194/acp-8-2405-2008, 2008.

954 Huang, G. L., Brook, R., Crippa, M., Janssens-Maenhout, G., Schieberle, C., Dore, C., Guizzardi, D.,
 955 Muntean, M., Schaaf, E., and Friedrich, R.: Speciation of anthropogenic emissions of non-methane
 956 volatile organic compounds: a global gridded data set for 1970-2012, *Atmospheric Chemistry and*
 957 *Physics*, 17, 7683-7701, 10.5194/acp-17-7683-2017, 2017.

958 Huang, X., Li, M., Li, J., and Song, Y.: A high-resolution emission inventory of crop burning in fields
 959 in China based on MODIS Thermal Anomalies/Fire products, *Atmos. Environ.*, 50, 9-15, doi:
 960 10.1016/j.atmosenv.2012.01.017, 2012.

961 Ip, H. S. S., Huang, X. H. H., and Yu, J. Z.: Effective Henry's law constants of glyoxal, glyoxylic acid,
 962 and glycolic acid, *Geophys. Res. Lett.*, 36, doi: 10.1029/2008GL036212, 2009.

963 Jenkin, M. E., Saunders, S. M., Wagner, V., and Pilling, M. J.: The tropospheric degradation of volatile
 964 organic compounds: a protocol for mechanism development, *Atmos. Environ.*, 31, 81-104,
 965 doi:10.1016/S1352-2310(96)00105-7, 1997.

966 Jenkin, M. E., Saunders, S. M., Wagner, V., and Pilling, M. J.: Protocol for the development of the
 967 Master Chemical Mechanism, MCM v3 (Part B): tropospheric degradation of aromatic volatile organic
 968 compounds, *Atmos. Chem. and Phys.*, 3, 181-193, doi:10.5194/acp-3-181-2003, 2003.

969 Jenkin, M. E., Young, J. C., and Rickard, A. R.: The MCM v3.3.1 degradation scheme for isoprene,
 970 Atmos. Chem. Phys., 15, 11433-11459, doi: 10.5194/acp-15-11433-2015, 2015.

971 Kurokawa, J., Ohara, T., Morikawa, T., Hanayama, S., Janssens-Maenhout, G., Fukui, T., Kawashima,
 972 K., and Akimoto, H.: Emissions of air pollutants and greenhouse gases over Asian regions during
 973 2000-2008: Regional Emission inventory in ASia (REAS) version 2, Atmos. Chem. Phys., 13,
 974 11019-11058, doi:10.5194/acp-13-11019-2013, 2013.

975 Lee, H., Ryu, J., Irie, H., Jang, S.-H., Park, J., Choi, W., and Hong, H.: Investigations of the Diurnal
 976 Variation of Vertical HCHO Profiles Based on MAX-DOAS Measurements in Beijing: Comparisons
 977 with OMI Vertical Column Data, Atmosphere, 6, 1816-1832, doi: 10.3390/atmos6111816, 2015.

978 Lerot, C., Stavrakou, T., De Smedt, I., Muller, J. F., and Van Roozendaal, M.: Glyoxal vertical columns
 979 from GOME-2 backscattered light measurements and comparisons with a global model, Atmos. Chem.
 980 Phys., 10, 12059-12072, doi: 10.5194/acp-10-12059-2010, 2010.

981 Li, D., and Bian, J. C.: Observation of a Summer Tropopause Fold by Ozonesonde at Changchun,
 982 China: Comparison with Reanalysis and Model Simulation, Adv. Atmos. Sci., 32, 1354-1364, doi:
 983 10.1007/s00376-015-5022-x, 2015.

984 Li, J., Wang, Z. F., Akimoto, H., Gao, C., Pochanart, P., and Wang, X. Q.: Modeling study of ozone
 985 seasonal cycle in lower troposphere over east Asia, J. Geophys. Res. Atmos., 112, doi:
 986 10.1029/2006JD008209, 2007.

987 Li, J. Y., Mao, J. Q., Min, K. E., Washenfelder, R. A., Brown, S. S., Kaiser, J., Keutsch, F. N., Volkamer,
 988 R., Wolfe, G. M., Hanisco, T. F., Pollack, I. B., Ryerson, T. B., Graus, M., Gilman, J. B., Lerner, B. M.,
 989 Warneke, C., de Gouw, J. A., Middlebrook, A. M., Liao, J., Welti, A., Henderson, B. H., McNeill, V. F.,
 990 Hall, S. R., Ullmann, K., Donner, L. J., Paulot, F., and Horowitz, L. W.: Observational constraints on
 991 glyoxal production from isoprene oxidation and its contribution to organic aerosol over the Southeast
 992 United States, J. Geophys. Res. Atmos., 121, 9849-9861, doi: 10.1002/2016JD025331, 2016.

993 Li, M., Zhang, Q., Streets, D. G., He, K. B., Cheng, Y. F., Emmons, L. K., Huo, H., Kang, S. C., Lu, Z.,
 994 Shao, M., Su, H., Yu, X., and Zhang, Y.: Mapping Asian anthropogenic emissions of non-methane
 995 volatile organic compounds to multiple chemical mechanisms, Atmos. Chem. Phys., 14, 5617-5638,
 996 doi:10.5194/acp-14-5617-2014, 2014.

997 Li, M., Zhang, Q., Kurokawa, J. I., Woo, J. H., He, K., Lu, Z., Ohara, T., Song, Y., Streets, D. G.,
 998 Carmichael, G. R., Cheng, Y., Hong, C., Huo, H., Jiang, X., Kang, S., Liu, F., Su, H., and Zheng, B.:
 999 MIX: a mosaic Asian anthropogenic emission inventory under the international collaboration
 1000 framework of the MICS-Asia and HTAP, Atmos. Chem. Phys., 17, 935-963,
 1001 doi:10.5194/acp-17-935-2017, 2017.

1002 Li, X., Brauers, T., Hofzumahaus, A., Lu, K., Li, Y. P., Shao, M., Wagner, T., and Wahner, A.:
 1003 MAX-DOAS measurements of NO₂, HCHO and CHOCHO at a rural site in Southern China, Atmos.
 1004 Chem. Phys., 13, 2133-2151, doi: 10.5194/acp-13-2133-2013, 2013.

1005 Liao, H., Henze, D. K., Seinfeld, J. H., Wu, S. L., and Mickley, L. J.: Biogenic secondary organic

1006 aerosol over the United States: Comparison of climatological simulations with observations, *Journal of*
1007 *Geophysical Research*, 112, doi:10.1029/2006JD007813, 2007.

1008 Liggio, J., Li, S. M., and McLaren, R.: Reactive uptake of glyoxal by particulate matter, *J. Geophys.*
1009 *Res. Atmos.*, 110, doi: 10.1029/2004JD005113, 2005.

1010 Liu, M., Song, Y., Yao, H., Kang, Y., Li, M., Huang, X., and Hu, M.: Estimating emissions from
1011 agricultural fires in the North China Plain based on MODIS fire radiative power, *Atmos. Environ.*, 112,
1012 326-334, doi: 10.1016/j.atmosenv.2015.04.058, 2015.

1013 Liu, Z., Wang, Y., Vrekoussis, M., Richter, A., Wittrock, F., Burrows, J. P., Shao, M., Chang, C.-C., Liu,
1014 S.-C., Wang, H., and Chen, C.: Exploring the missing source of glyoxal (CHOCHO) over China,
1015 *Geophys. Res. Lett.*, 39, doi:10.1029/2012gl051645, 2012.

1016 Mao, J. Q., Paulot, F., Jacob, D. J., Cohen, R. C., Crounse, J. D., Wennberg, P. O., Keller, C. A.,
1017 Hudman, R. C., Barkley, M. P., and Horowitz, L. W.: Ozone and organic nitrates over the eastern
1018 United States: Sensitivity to isoprene chemistry, *J. Geophys. Res. Atmos.*, 118, 11256-11268, doi:
1019 10.1002/jgrd.50817, 2013.

1020 Marais, E. A., Jacob, D. J., Kurosu, T. P., Chance, K., Murphy, J. G., Reeves, C., Mills, G., Casadio, S.,
1021 Millet, D. B., Barkley, M. P., Paulot, F., and Mao, J.: Isoprene emissions in Africa inferred from OMI
1022 observations of formaldehyde columns, *Atmos. Chem. Phys.*, 12, 6219-6235, doi:
1023 10.5194/acp-12-6219-2012, 2012.

1024 Marais, E. A., Jacob, D. J., Guenther, A., Chance, K., Kurosu, T. P., Murphy, J. G., Reeves, C. E., and
1025 Pye, H. O. T.: Improved model of isoprene emissions in Africa using Ozone Monitoring Instrument
1026 (OMI) satellite observations of formaldehyde: implications for oxidants and particulate matter, *Atmos.*
1027 *Chem. Phys.*, 14, 7693-7703, doi: 10.5194/acp-14-7693-2014, 2014a.

1028 Marais, E. A., Jacob, D. J., Wecht, K., Lerot, C., Zhang, L., Yu, K., Kurosu, T. P., Chance, K., and
1029 Sauvage, B.: Anthropogenic emissions in Nigeria and implications for atmospheric ozone pollution: A
1030 view from space, *Atmos. Environ.*, 99, 32-40, doi: 10.1016/j.atmosenv.2014.09.055, 2014b.

1031 Mijling, B., van der A, R. J., and Zhang, Q.: Regional nitrogen oxides emission trends in East Asia
1032 observed from space, *Atmospheric Chemistry and Physics*, 13, 12003-12012, doi:
1033 10.5194/acp-13-12003-2013, 2013.

1034 Millet, D. B., Jacob, D. J., Turquety, S., Hudman, R. C., Wu, S., Fried, A., Walega, J., Heikes, B. G.,
1035 Blake, D. R., Singh, H. B., Anderson, B. E., and Clarke, A. D.: Formaldehyde distribution over North
1036 America: Implications for satellite retrievals of formaldehyde columns and isoprene emission, *J.*
1037 *Geophys. Res.*, 111, doi: 10.1029/2005jd006853, 2006.

1038 Millet, D. B., Jacob, D. J., Boersma, K. F., Fu, T.-M., Kurosu, T. P., Chance, K., Heald, C. L., and
1039 Guenther, A.: Spatial distribution of isoprene emissions from North America derived from
1040 formaldehyde column measurements by the OMI satellite sensor, *J. Geophys. Res.*, 113, doi:
1041 10.1029/2007jd008950, 2008.

1042 Myriokefalitakis, S., Vrekoussis, M., Tsigaridis, K., Wittrock, F., Richter, A., Bruehl, C., Volkamer, R.,
 1043 Burrows, J. P., and Kanakidou, M.: The influence of natural and anthropogenic secondary sources on
 1044 the glyoxal global distribution, *Atmos. Chem. Phys.*, 8, 4965-4981, doi: 10.5194/acp-8-4965-2008,
 1045 2008.

1046 Nishino, N., Arey, J., and Atkinson, R.: Formation Yields of Glyoxal and Methylglyoxal from the
 1047 Gas-Phase OH Radical-Initiated Reactions of Toluene, Xylenes, and Trimethylbenzenes as a Function
 1048 of NO₂ Concentration, *J. Phys. Chem. A*, 114, 10140, doi: 10.1021/jp105112h, 2010.

1049 Olivier, J. G. J., Bouwman, A. F., Berdowski, J. J. M., Veldt, C., Bloos, J. P. J., Visschedijk, A. J. H.,
 1050 van der Maas, C. W. M., and Zandveld, P. Y. J.: Sectoral emission inventories of greenhouse gases for
 1051 1990 on a per country basis as well as on 1°×1°, *Environ. Sci. Policy*, 2, 241-263,
 1052 doi:10.1016/S1462-9011(99)00027-1, 1999.

1053 Olivier, J. G. J., Berdowski, J. J. M., Peters, J. A. H. W., Bakker, J., Visschedijk, A. J. H., and Bloos,
 1054 J.-P. J.: Applications of EDGAR, Including a description of EDGAR 3.0: reference database with trend
 1055 data for 1970–1995, RIVM report no. 773301 001/ NOP report no. 410200 051, RIVM, Bilthoven,
 1056 2001.

1057 Olivier, J. G. J.: Part III: Greenhouse gas emissions. 1. Shares and trends in greenhouse gas emissions;
 1058 2. Sources and methods: greenhouse gas emissions for 1990 and 1995 in “CO₂ emissions from fuel
 1059 combustion 1971–2000”, International Energy Agency, Paris, ISBN 92-64-09794-5, 1–31, 1–31, 2002.

1060 Palmer, P. I., Jacob, D. J., Fiore, A. M., Martin, R. V., Chance, K., and Kurosu, T. P.: Mapping isoprene
 1061 emissions over North America using formaldehyde column observations from space, *J. Geophys. Res.*
 1062 *Atmos.*, 108, doi: 10.1029/2002jd002153, 2003.

1063 Palmer, P. I., Abbot, D. S., Fu, T.-M., Jacob, D. J., Chance, K., Kurosu, T. P., Guenther, A., Wiedinmyer,
 1064 C., Stanton, J. C., Pilling, M. J., Pressley, S. N., Lamb, B., and Sumner, A. L.: Quantifying the seasonal
 1065 and interannual variability of North American isoprene emissions using satellite observations of the
 1066 formaldehyde column, *J. Geophys. Res.*, 111, doi: 10.1029/2005jd006689, 2006.

1067 Paulot, F., Crounse, J. D., Kjaergaard, H. G., Kroll, J. H., Seinfeld, J. H., and Wennberg, P. O.: Isoprene
 1068 photooxidation: new insights into the production of acids and organic nitrates, *Atmos. Chem. Phys.*, 9,
 1069 1479-1501, doi: 10.5194/acp-9-1479-2009, 2009a.

1070 Paulot, F., Crounse, J. D., Kjaergaard, H. G., Kurten, A., St Clair, J. M., Seinfeld, J. H., and Wennberg,
 1071 P. O.: Unexpected Epoxide Formation in the Gas-Phase Photooxidation of Isoprene, *Science*, 325,
 1072 730-733, doi: 10.1126/science.1172910, 2009b.

1073 Platt, U., Perner, D., and Pätz, H. W.: Simultaneous measurement of atmospheric CH₂O, O₃, and NO₂
 1074 by differential optical absorption, *J. Geophys. Res. Oceans*, 84, 6329-6335,
 1075 doi:10.1029/JC084iC10p06329, 1979.

1076 Pye, H. O. T., and Seinfeld, J. H.: A global perspective on aerosol from low-volatility organic
 1077 compounds, *Atmos. Chem. Phys.*, 10, 4377-4401, doi:10.5194/acp-10-4377-2010.

1078 Qiu, K., Yang, L., Lin, J., Wang, P., Yang, Y., Ye, D., and Wang, L.: Historical industrial emissions of
 1079 non-methane volatile organic compounds in China for the period of 1980–2010, *Atmos. Environ.*, 86,
 1080 102–112, doi:10.1016/j.atmosenv.2013.12.026, 2014.

1081 Qu, Z., Henze, D. K., Capps, S. L., Wang, Y., Xu, X. G., Wang, J., and Keller, M.: Monthly top-down
 1082 NO_x emissions for China (2005–2012): A hybrid inversion method and trend analysis, *J. Geophys. Res.*
 1083 *Atmos.*, 122, 4600–4625, doi: 10.1002/2016JD025852, 2017.

1084 Robinson, A. L., Donahue, N. M., Shrivastava, M. K., Weitkamp, E. A., Sage, A. M., Grieshop, A. P.,
 1085 Lane, T. E., Pierce, J. R., and Pandis, S. N.: Rethinking organic aerosols: Semivolatile emissions and
 1086 photochemical aging, *Science*, 315, 1259–1262, doi: 10.1126/science.1133061 2007.

1087 Rodgers, C. D.: *Inverse methods for atmospheric sounding: theory and practice*, World Scientific,
 1088 Singapore, 2000.

1089 Sandu, A., Daescu, D. N., and Carmichael, G. R.: Direct and adjoint sensitivity analysis of chemical
 1090 kinetic systems with KPP: Part I - theory and software tools, *Atmos. Environ.*, 37, 5083–5096,
 1091 doi:10.1016/j.atmosenv.2003.08.019, 2003.

1092 Saunders, S. M., Jenkin, M. E., Derwent, R. G., and Pilling, M. J.: Protocol for the development of the
 1093 Master Chemical Mechanism, MCM v3 (Part A): tropospheric degradation of non-aromatic volatile
 1094 organic compounds, *Atmos. Chem. Phys.*, 3, 181–193, doi: 10.5194/acp-3-161-2003, 2003.

1095 Schultz, M. G., Backman, L., and Balkanski, Y.: REanalysis of the TROpospheric chemical
 1096 composition over the past 40 years (RETRO): A long-term global modeling study of tropospheric
 1097 chemistry, Jülich/Hamburg, Germany, 48/2007 report on Earth System Science of the Max Planck
 1098 Institute for Meteorology, Hamburg, <http://retro.enes.org>, ISSN 1614-1199, 2007.

1099 Shim, C., Wang, Y., Choi, Y., Palmer, P. I., Abbot, D. S., and Chance, K.: Constraining global isoprene
 1100 emissions with Global Ozone Monitoring Experiment (GOME) formaldehyde column measurements, *J.*
 1101 *Geophys. Res.*, 110, doi: 10.1029/2004jd005629, 2005.

1102 Sindelarova, K., Granier, C., Bouarar, I., Guenther, A., Tilmes, S., Stavrakou, T., Muller, J. F., Kuhn, U.,
 1103 Stefani, P., and Knorr, W.: Global data set of biogenic VOC emissions calculated by the MEGAN
 1104 model over the last 30 years, *Atmospheric Chemistry and Physics*, 14, 9317–9341,
 1105 doi:10.5194/acp-14-9317-2014, 2014.

1106 Spurr, R.: LIDORT and VLIDORT: Linearized pseudo-spherical scalar and vector discrete ordinate
 1107 radiative transfer models for use in remote sensing retrieval problems, in: *Light Scattering Reviews*,
 1108 edited by: Kokhanovsky, A., Springer, 3, 229–275, 2008.

1109
 1110 Spurr, R. J. D.: VLIDORT: A linearized pseudo-spherical vector discrete ordinate radiative transfer
 1111 code for forward model and retrieval studies in multilayer multiple scattering media, *J. Quant.*
 1112 *Spectrosc. Radiat. Transf.*, 102, 316–342, doi: 10.1016/j.jqsrt.2006.05.005, 2006.

1113 Stavrakou, T., Guenther, A., Razavi, A., Clarisse, L., Clerbaux, C., Coheur, P. F., Hurtmans, D.,
 1114 Karagulian, F., De Maziere, M., Vigouroux, C., Amelynck, C., Schoon, N., Laffineur, Q., Heinesch, B.,

1115 Aubinet, M., Rinsland, C., and Muller, J. F.: First space-based derivation of the global atmospheric
 1116 methanol emission fluxes, *Atmos. Chem. Phys.*, 11, 4873-4898, doi: 10.5194/acp-11-4873-2011, 2011.

1117 Stavrakou, T., Muller, J. F., Bauwens, M., De Smedt, I.: Sources and long-term trends of ozone
 1118 precursors to Asian Pollution, *Air Pollution in Eastern Asia : an integrated perspective*, eds. Bouarar,
 1119 I., Wang, X., Brasseur, G., Springer international Publishing, doi:10.1007/978-3-319-59489-7-8, pp.
 1120 167-189, 2017.

1121 Stavrakou, T., Muller, J. F., Bauwens, M., De Smedt, I., Lerot, C., Van Roozendaal, M., Coheur, P. F.,
 1122 Clerbaux, C., Boersma, K. F., van der, A. R., and Song, Y.: Substantial Underestimation of
 1123 Post-Harvest Burning Emissions in the North China Plain Revealed by Multi-Species Space
 1124 Observations, *Sci. Rep.*, 6, 32307, doi: 10.1038/srep32307, 2016.

1125 Stavrakou, T., Muller, J. F., Bauwens, M., De Smedt, I., Van Roozendaal, M., Guenther, A., Wild, M.,
 1126 and Xia, X.: Isoprene emissions over Asia 1979-2012: impact of climate and land-use changes, *Atmos.*
 1127 *Chem. and Phys.*, 14, 4587-4605, doi: 10.5194/acp-14-4587-2014, 2014.

1128 Stavrakou, T., Müller, J. F., Bauwens, M., De Smedt, I., Van Roozendaal, M., De Mazière, M.,
 1129 Vigouroux, C., Hendrick, F., George, M., Clerbaux, C., Coheur, P. F., and Guenther, A.: How consistent
 1130 are top-down hydrocarbon emissions based on formaldehyde observations from GOME-2 and OMI?,
 1131 *Atmos. Chem. Phys.*, 15, 11861-11884, doi: 10.5194/acp-15-11861-2015, 2015.

1132 Stavrakou, T., Muller, J. F., De Smedt, I., Van Roozendaal, M., Kanakidou, M., Vrekoussis, M.,
 1133 Wittrock, F., Richter, A., and Burrows, J. P.: The continental source of glyoxal estimated by the
 1134 synergistic use of spaceborne measurements and inverse modelling, *Atmos. Chem. Phys.*, 9, 8431-8446,
 1135 doi: 10.5194/acp-9-8431-2009, 2009a.

1136 Stavrakou, T., Muller, J. F., De Smedt, I., Van Roozendaal, M., van der Werf, G. R., Giglio, L., and
 1137 Guenther, A.: Global emissions of non-methane hydrocarbons deduced from SCIAMACHY
 1138 formaldehyde columns through 2003-2006, *Atmos. Chem. Phys.*, 9, 3663-3679,
 1139 doi:10.5194/acp-9-3663-2009, 2009b.

1140 Sun, L., Xue, L. K., Wang, T., Gao, J., Ding, A. J., Cooper, O. R., Lin, M. Y., Xu, P. J., Wang, Z., Wang,
 1141 X. F., Wen, L., Zhu, Y. H., Chen, T. S., Yang, L. X., Wang, Y., Chen, J. M., and Wang, W. X.:
 1142 Significant increase of summertime ozone at Mount Tai in Central Eastern China, *Atmos. Chem. Phys.*,
 1143 16, 10637-10650, doi: 10.5194/acp-16-10637-2016, 2016.

1144 van der Werf, G. R., Randerson, J. T., Giglio, L., Collatz, G. J., Mu, M., Kasibhatla, P. S., Morton, D.
 1145 C., DeFries, R. S., Jin, Y., and van Leeuwen, T. T.: Global fire emissions and the contribution of
 1146 deforestation, savanna, forest, agricultural, and peat fires (1997–2009), *Atmos. Chem. Phys.*, 10,
 1147 11707-11735, doi:10.5194/acp-10-11707-2010, 2010.

1148 van der Werf, G. R., Randerson, J. T., Giglio, L., van Leeuwen, T. T., Chen, Y., Rogers, B. M., Mu, M.
 1149 Q., van Marle, M. J. E., Morton, D. C., Collatz, G. J., Yokelson, R. J., and Kasibhatla, P. S.: Global fire
 1150 emissions estimates during 1997-2016, *Earth Syst Sci Data*, 9, 697-720, doi: 10.5194/essd-9-697-2017,
 1151 2017.

- 1152 van Donkelaar, A., Martin, R. V., Leaitch, W. R., Macdonald, A. M., Walker, T. W., Streets, D. G.,
1153 Zhang, Q., Dunlea, E. J., Jimenez, J. L., Dibb, J. E., Huey, L. G., Weber, R., and Andreae, M. O.:
1154 Analysis of aircraft and satellite measurements from the Intercontinental Chemical Transport
1155 Experiment (INTEX-B) to quantify long-range transport of East Asian sulfur to Canada, *Atmos. Chem.*
1156 *Phys.*, 8, 2999-3014, doi: 10.5194/acp-8-2999-2008, 2008.
- 1157 Vestreng, V.: Review and revision. Emission data reported to CLRTAP, Tech. rep., EMEP MSC-W,
1158 (available at: http://www.emep.int/mscw/mscw_publications.html#2003), 2003.
- 1159 Vlemmix, T., Hendrick, F., Pinardi, G., Smedt, I., De Fayt, C., Hermans, C., Pitters, A., Wang, P., and
1160 Levelt, P.: MAX-DOAS observations of aerosols, formaldehyde and nitrogen dioxide in the Beijing
1161 area: comparison of two profile retrieval, *Atmos. Meas. Tech.*, 2, 941–963,
1162 doi:10.5194/amt-8-941-2015, 2015.
- 1163 Volkamer, R.: Primary and Secondary Glyoxal Formation from Aromatics: Experimental Evidence for
1164 the Bicycloalkyl-Radical Pathway from Benzene, Toluene, and p-Xylene, *J. Phys. Chem.*, 105, 7865,
1165 doi:10.1021/jp010152w, 2001.
- 1166 Vrekoussis, M., Wittrock, F., Richter, A., and Burrows, J. P.: GOME-2 observations of oxygenated
1167 VOCs: what can we learn from the ratio glyoxal to formaldehyde on a global scale?, *Atmos. Chem.*
1168 *Phys.*, 10, 10145-10160, doi: 10.5194/acp-10-10145-2010, 2010.
- 1169 Wang, F., An, J., Li, Y., Tang, Y., Lin, J., Qu, Y., Chen, Y., Zhang, B., and Zhai, J.: Impacts of
1170 uncertainty in AVOC emissions on the summer ROx budget and ozone production rate in the three most
1171 rapidly-developing economic growth regions of China, *Adv. Atmos. Sci.*, 31, 1331-1342, doi:
1172 10.1007/s00376-014-3251-z, 2014.
- 1173 Wang, H. Q., Ma, J. M., Shen, Y. J., and Wang, Y. A.: Assessment of Ozone Variations and
1174 Meteorological Influences at a Rural Site in Northern Xinjiang, *Bull. Environ. Contam. Toxicol.*, 94,
1175 240-246, doi: 10.1007/s00128-014-1451-y, 2015.
- 1176 Wang, P., Stammes, P., R., v. d. A., Pinardi, G., and Roozendael, M. V.: FRESCO+: an improved O2
1177 A-band cloud retrieval algorithm for tropospheric trace gas retrievals, *Atmos. Chem. Phys.*, 8,
1178 6565-6576, doi: 10.5194/acp-8-6565-2008, 2008.
- 1179 Wang, Y., Konopka, P., Liu, Y., Chen, H., Muller, R., Ploger, F., Riese, M., Cai, Z., and Lu, D.:
1180 Tropospheric ozone trend over Beijing from 2002-2010: ozonesonde measurements and modeling
1181 analysis, *Atmos. Chem. Phys.*, 12, 8389-8399, doi: 10.5194/acp-12-8389-2012, 2012.
- 1182 Wang, Y., Beirle, S., Lampel, J., Koukouli, M., De Smedt, I., Theys, N., Li, A., Wu, D. X., Xie, P. H.,
1183 Liu, C., Van Roozendael, M., Stavrakou, T., Muller, J. F., and Wagner, T.: Validation of OMI,
1184 GOME-2A and GOME-2B tropospheric NO2, SO2 and HCHO products using MAX-DOAS
1185 observations from 2011 to 2014 in Wuxi, China: investigation of the effects of priori profiles and
1186 aerosols on the satellite products, *Atmos. Chem. Phys.*, 17, 5007-5033, doi: 10.5194/acp-17-5007-2017,
1187 2017.
- 1188 Wei, W., Wang, S., Chatani, S., Klimont, Z., Cofala, J., and Hao, J.: Emission and speciation of

1189 non-methane volatile organic compounds from anthropogenic sources in China, *Atmos. Environ.*, 42,
1190 4976-4988, doi:10.1016/j.atmosenv.2008.02.044, 2008.

1191 Wells, K. C., Millet, D. B., Hu, L., Cady-Pereira, K. E., Xiao, Y., Shephard, M. W., Clerbaux, C. L.,
1192 Clarisse, L., Coheur, P. F., Apel, E. C., de Gouw, J., Warneke, C., Singh, H. B., Goldstein, A. H., and
1193 Sive, B. C.: Tropospheric methanol observations from space: retrieval evaluation and constraints on the
1194 seasonality of biogenic emissions, *Atmos. Chem. Phys.*, 12, 5897-5912, doi:
1195 10.5194/acp-12-5897-2012, 2012.

1196 Wiedinmyer, C., Akagi, S. K., Yokelson, R. J., Emmons, L. K., Al-Saadi, J. A., Orlando, J. J., and Soja,
1197 A. J.: The Fire INventory from NCAR (FINN): a high resolution global model to estimate the
1198 emissions from open burning, *Geosci. Model Dev.*, 4, 625-641, doi: 10.5194/gmd-4-625-2011, 2011.

1199 Wittrock, F., Richter, A., Oetjen, H., Burrows, J. P., Kanakidou, M., Myriokefalitakis, S., Volkamer, R.,
1200 Beirle, S., Platt, U., and Wagner, T.: Simultaneous global observations of glyoxal and formaldehyde
1201 from space, *Geophys. Res. Lett.*, 33, doi: 10.1029/2006gl026310, 2006.

1202 Wu, R., Bo, Y., Li, J., Li, L., Li, Y., and Xie, S.: Method to establish the emission inventory of
1203 anthropogenic volatile organic compounds in China and its application in the period 2008–2012, *Atmos.*
1204 *Environ.*, 127, 244-254, doi:10.1016/j.atmosenv.2015.12.015, 2016.

1205 Xu, W. Y., Lin, W. L., Xu, X. B., Tang, J., Huang, J. Q., Wu, H., and Zhang, X. C.: Long-term trends of
1206 surface ozone and its influencing factors at the Mt Waliguan GAW station, China - Part 1: Overall
1207 trends and characteristics, *Atmos. Chem. Phys.*, 16, 6191-6205, doi: 10.5194/acp-16-6191-2016, 2016.

1208 Xu, X., Lin, W., Wang, T., Yan, P., Tang, J., Meng, Z., and Wang, Y.: Long-term trend of surface ozone
1209 at a regional background station in eastern China 1991-2006: enhanced variability, *Atmos. Chem. Phys.*,
1210 8, 2595-2607, doi: 10.5194/acp-8-2595-2008, 2008.

1211 Zhang, J. M., Wang, T., Ding, A. J., Zhou, X. H., Xue, L. K., Poon, C. N., Wu, W. S., Gao, J., Zuo, H.
1212 C., Chen, J. M., Zhang, X. C., and Fan, S. J.: Continuous measurement of peroxyacetyl nitrate (PAN) in
1213 suburban and remote areas of western China, *Atmos. Environ.*, 43, 228-237, doi:
1214 10.1016/j.atmosenv.2008.09.070, 2009.

1215 Zhang, Q., Streets, D. G., Carmichael, G. R., He, K. B., Huo, H., Kannari, A., Klimont, Z., Park, I. S.,
1216 Reddy, S., Fu, J. S., Chen, D., Duan, L., Lei, Y., Wang, L. T., and Yao, Z. L.: Asian emissions in 2006
1217 for the NASA INTEX-B mission, *Atmos. Chem. Phys.*, 9, 5131-5153, 10.5194/acp-9-5131-2009, 2009.

1218 Zhang, X. Y., Wang, Y. Q., Niu, T., Zhang, X. C., Gong, S. L., Zhang, Y. M., and Sun, J. Y.:
1219 Atmospheric aerosol compositions in China: spatial/temporal variability, chemical signature, regional
1220 haze distribution and comparisons with global aerosols, *Atmospheric Chemistry and Physics*, 12,
1221 779-799, doi:10.5194/acp-12-779-2012, 2012.

1222 Zhao, Y., Nielsen, C. P., Lei, Y., McElroy, M. B., and Hao, J.: Quantifying the uncertainties of a
1223 bottom-up emission inventory of anthropogenic atmospheric pollutants in China, *Atmos. Chem. Phys.*,
1224 11, 2295-2308, doi:10.5194/acp-11-2295-2011, 2011.

1225 Zheng, J. Y., Zhong, L. J., Wang, T., Louie, P. K. K., and Li, Z. C.: Ground-level ozone in the Pearl
 1226 River Delta region: Analysis of data from a recently established regional air quality monitoring
 1227 network, *Atmos. Environ.*, 44, 814-823, doi: 10.1016/j.atmosenv.2009.11.032, 2010.

1228 Zhu, L., Jacob, D. J., Mickley, L. J., Marais, E. A., Cohan, D. S., Yoshida, Y., Duncan, B. N., González
 1229 Abad, G., and Chance, K. V.: Anthropogenic emissions of highly reactive volatile organic compounds
 1230 in eastern Texas inferred from oversampling of satellite (OMI) measurements of HCHO columns,
 1231 *Environ. Res. Lett.*, 9, 114004, doi: 10.1088/1748-9326/9/11/114004, 2014.

1232 Zhu, L., Jacob, D. J., Kim, P. S., Fisher, J. A., Yu, K., Travis, K. R., Mickley, L. J., Yantosca, R. M.,
 1233 Sulprizio, M. P., De Smedt, I., González Abad, G., Chance, K., Li, C., Ferrare, R., Fried, A., Hair, J. W.,
 1234 Hanisco, T. F., Richter, D., Jo Scarino, A., Walega, J., Weibring, P., and Wolfe, G. M.: Observing
 1235 atmospheric formaldehyde (HCHO) from space: validation and intercomparison of six retrievals from
 1236 four satellites (OMI, GOME2A, GOME2B, OMPS) with SEAC⁴RS aircraft observations over the
 1237 southeast US, *Atmos. Chem. Phys.*, 16, 13477-13490, doi: 10.5194/acp-16-13477-2016, 2016.

1238

1239

Table 1 Inversion experiments to constrain Chinese NMVOC emissions

Inversion experiments	Observational constraints from satellites [\pm uncertainties]	Annual Chinese NMVOC emission estimates [Tg y ⁻¹]			
		Anthropogenic	Biogenic	Biomass burning	Total
		<i>A priori</i> emission estimates [uncertainty]			
		18.8 (5.4 for aromatics) ^a [factor of two uncertainty]	17.3 (7.5 for isoprene) ^b [\pm 55% uncertainty]	2.27 [factor of three uncertainty] ^c	38.3
		<i>A posteriori</i> emission estimates [range of estimates]			
IE-1	GOME-2A formaldehyde [\pm 90%] and glyoxal [\pm 150%]	17.8 (5.8 for aromatics)	20.0 (9.8 for isoprene)	2.27	40.1
IE-2	OMI formaldehyde [\pm 90%] and glyoxal [\pm 150%]	16.4 (5.5 for aromatics)	12.2 (5.4 for isoprene)	2.08	30.7
IE-3	GOME-2A formaldehyde \times 170% [\pm 90%]	23.6 (6.6 for aromatics)	22.8 (11.3 for isoprene)	3.13	49.5
IE-4	OMI glyoxal [\pm 150%]	23.0 (7.9 for aromatics)	21.6 (11.7 for isoprene)	2.43	47.0
Our top-down estimates		20.2 ^d [16.4 - 23.6] (6.5 ^d [5.5 - 7.9] for aromatics)	19.2 ^d [12.2 – 22.8] (9.6 ^d [5.4 – 11.7] for isoprene)	2.48 ^d [2.08 – 3.13]	41.9 ^d [30.7 – 49.5]

1240

^a From Li et al. (2017)

1241

^b From Guenther et al. (2006).

1242

^c Compiled from the emission estimated by van der Werf et al. (2010) plus a scaling of the emission estimated by Huang et al. (2012). See text (section 2.2) for details.

1244

^d Average of top-down estimates from the four inversion experiments.

1245

1246

1247

Table 2 Comparison of Chinese annual NMVOC emission estimates for the years 2000 to 2014

Literature	Target year	NMVOC [Tg y ⁻¹]				
		Anthropogenic		Biogenic		Biomass burning
		Total	Aromatics	Total	Isoprene	
<i>Bottom-up estimates</i>						
Bo et al. (2008) ^a	2005	12.7				3.8 ^d
Zhang et al. (2009) ^a	2006	23.2 (±68%)	2.4			
Cao et al. (2011) ^a	2007	35.46				
Huang et al. (2017) ^a	2007	24.6				
Granier et al. (2017) ^a	2007	29.0				
Kurokawa et al. (2013) ^a	2008	27.1 (±46%)				
Li et al. (2017) ^a	2010	23.6	5.4			
Wu et al. (2016) ^a	2008	18.62				3.83 ^d
	2009	21.8				3.32 ^d
	2010	23.83				3.75 ^d
	2011	24.78				3.76 ^d
	2012	25.65				4.20 ^d
Huang et al. (2012) ^a	2006					2.2 (1.08 to 3.46)
van der Werf et al. (2010)	2007					0.47
van der Werf et al. (2017) ^a	2007					0.91
Sindelarova et al. (2014)	2005				9.9	
Guenther et al.(2006)	2007			17.3 ^e	7.5 ^e	
Stavrakou et al. (2014)	2007				7.6	
<i>Top-down estimates</i>						
Fu et al. (2007)	2000	4.27 ^g		12.7		5.1
Liu et al. (2012) ^b	2007	34.2	13.4			
Stavrakou et al. (2014)	2007				8.6	
Stavrakou et al. (2015) ^c	2010	20.6 to 24.6			5.9 to 6.5	2.0 to 2.7
Stavrakou et al. (2017) ^c	2005	24.4			5.8 (average of emissions from 2005 to 2014)	
	2006	24.0				
	2007	26.7				
	2008	25.9				
	2009	26.5				
	2010	26.1				
	2011	25.5				
	2012	25.6				
	2013	27.7				
	2014	27.8				
This work	2007	20.2 ^f (16.4 - 23.6)	6.5 ^f (5.5 - 7.9)	19.2 ^f (12.2 - 22.8)	9.6 ^f (5.4 - 11.7)	2.48 ^f (2.08 – 3.13)

1249

1250 ^aThese emission estimates included some NMVOC species which were not precursors to formaldehyde or glyoxal
1251 and therefore not included in this work. See color keys in Figure 2 for NMVOC species whose emissions were
1252 included in this work.

1253 ^b Used SCIAMACHY-observed glyoxal VCDs as constraints.

1254 ^c Used GOME-2A-observed and OMI-observed formaldehyde VCDs as constraints.

1255 ^d Consisted of emissions from open burning of crop residues and from biofuel burning.

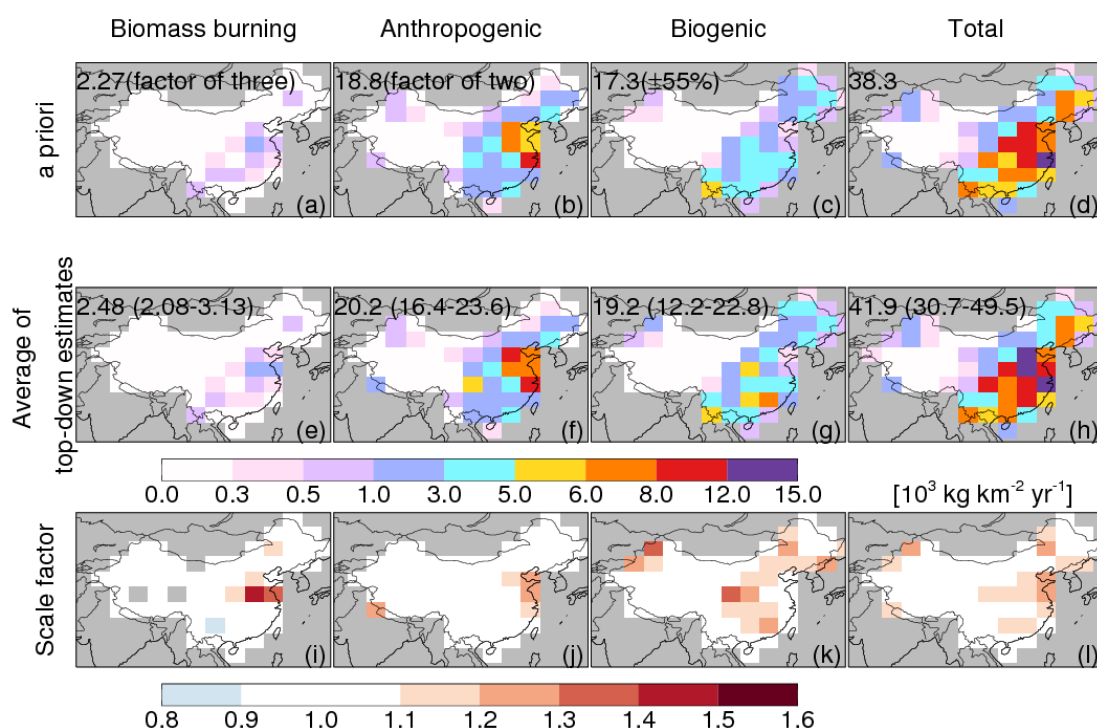
1256 ^e Calculated by the GEOS-Chem model using GEOS-5 meteorological data.

1257 ^f Average of top-down estimates from four inversion experiments.

1258 ^g Only anthropogenic emissions of reactive alkenes, formaldehyde, and xylenes from northeastern, northern,
1259 central and southern China were included

1260

1261



1263

1264 **Figure 1. Spatial distributions of annual NMVOC emissions from China. (a)-(d): The *a priori* annual**
 1265 **NMVOC emission estimates from (a) biomass burning, (b) anthropogenic, (c) biogenic, and (d) total sources.**
 1266 **(e)-(h): The average of our four sets of top-down estimates of annual NMVOC emissions. Annual Chinese**
 1267 **total emission estimates are shown inset in units of $[\text{Tg y}^{-1}]$. The uncertainties of the *a priori* emission**
 1268 **estimates and the range of top-down emission estimates are shown in parentheses. (i)-(l): Scale factors for**
 1269 **our averaged top-down estimates relative to the *a priori* estimates.**
 1270

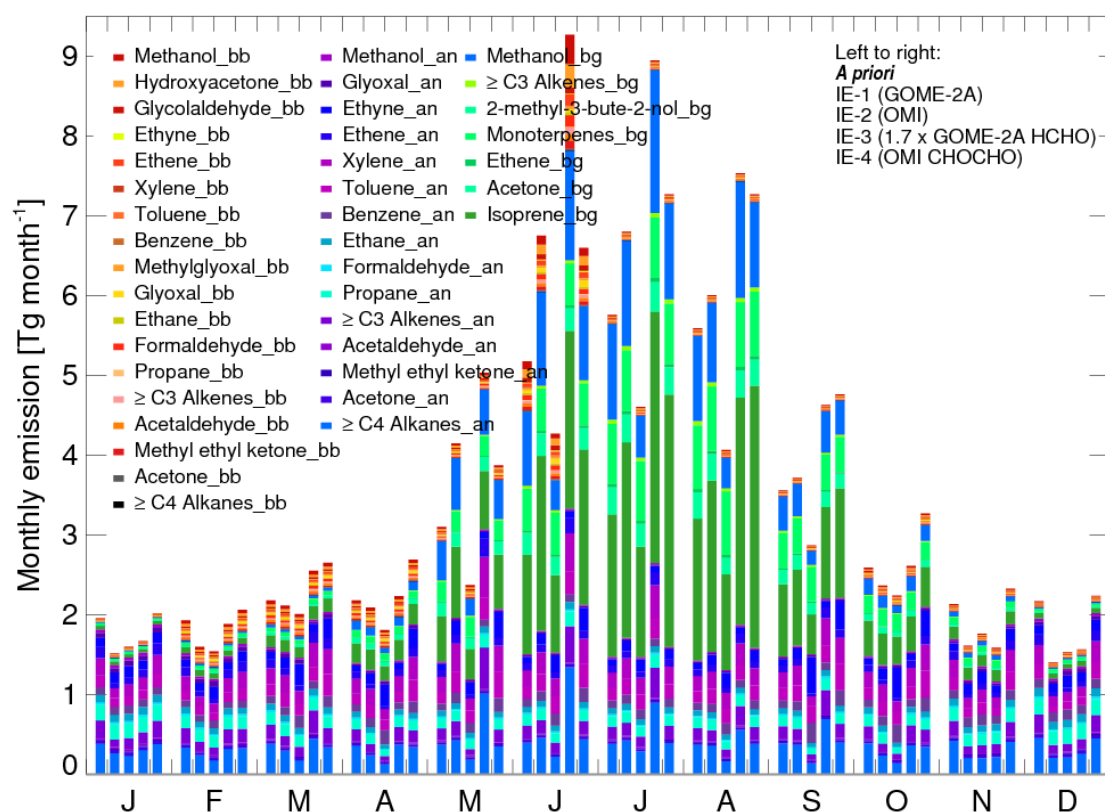
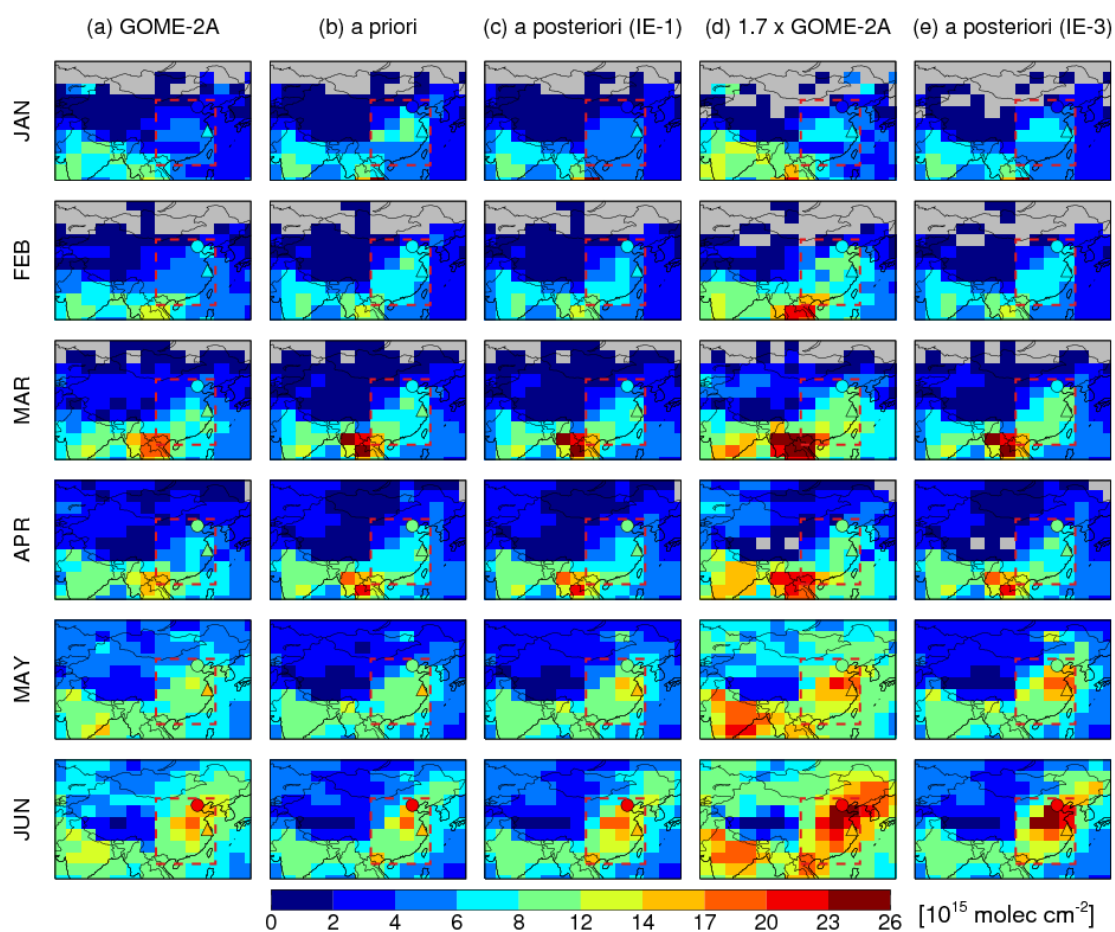


Figure 2. Estimates of monthly Chinese NMVOC emissions. For each month, the bars from left to right represent: the *a priori* emission estimates and the *a posteriori* emission estimates from IE-1, IE-2, IE-3, and IE-4, respectively. Color keys for NMVOC species are shown inset, with the suffixes of 'bb', 'an' and 'bg' indicating emissions from biomass burning, anthropogenic, and biogenic activities, respectively.

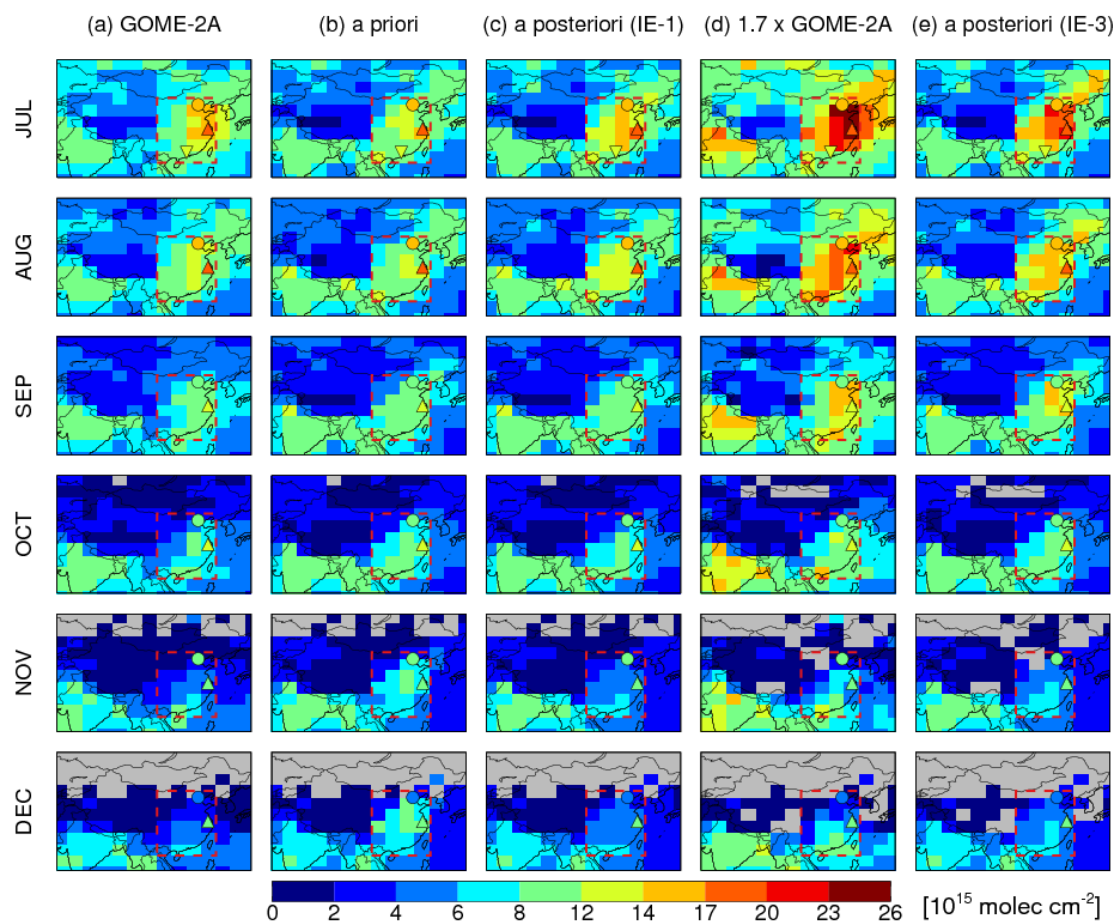


1279

1280 **Figure 3. Monthly mean formaldehyde VCDs over China from January to June. For each month, the panels**
 1281 **from left to right show: (a) formaldehyde VCDs observed by GOME-2A, (b) formaldehyde VCDs simulated**
 1282 **by the model using *a priori* emission estimates, (c) the *a posteriori* formaldehyde VCDs from IE-1, (d)**
 1283 **GOME-2A formaldehyde VCDs scaled by a factor of 1.7, and (e) the *a posteriori* formaldehyde VCDs from**
 1284 **IE-3. All model results were sampled at GOME-2A overpass time. Also shown are ground-based**
 1285 **MAX-DOAS measurements at 9:30 local time at Xianghe (monthly mean, circles) and Wuxi (bimonthly**
 1286 **mean, upward triangles).**

1287

1288



1289

1290

1291

1292

Figure 4. Same as Figure 3 except for July to December. Also shown are ground-based MAX-DOAS measurements at 9:30 local time at Back Garden (July mean, inverted triangles).

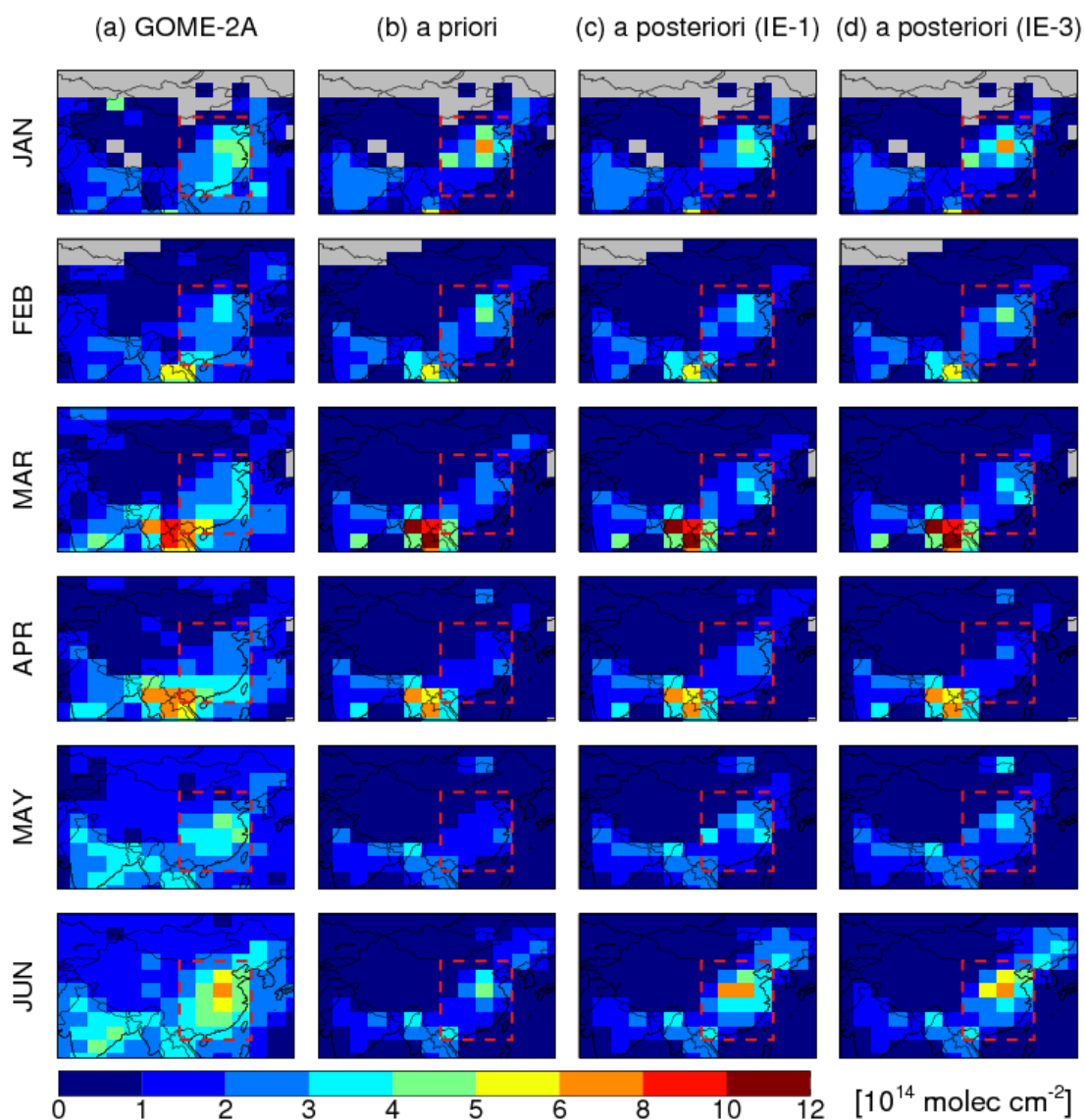


Figure 5. Monthly mean glyoxal VCDs over China from January to June. For each month, the panels from left to right show: (a) glyoxal VCDs observed by GOME-2A, (b) glyoxal VCDs simulated by the model using *a priori* emission estimates, (c) the *a posteriori* glyoxal VCDs from IE-1, and (d) the *a posteriori* glyoxal VCDs from IE-3. All model results were sampled at GOME-2A overpass time.

1301

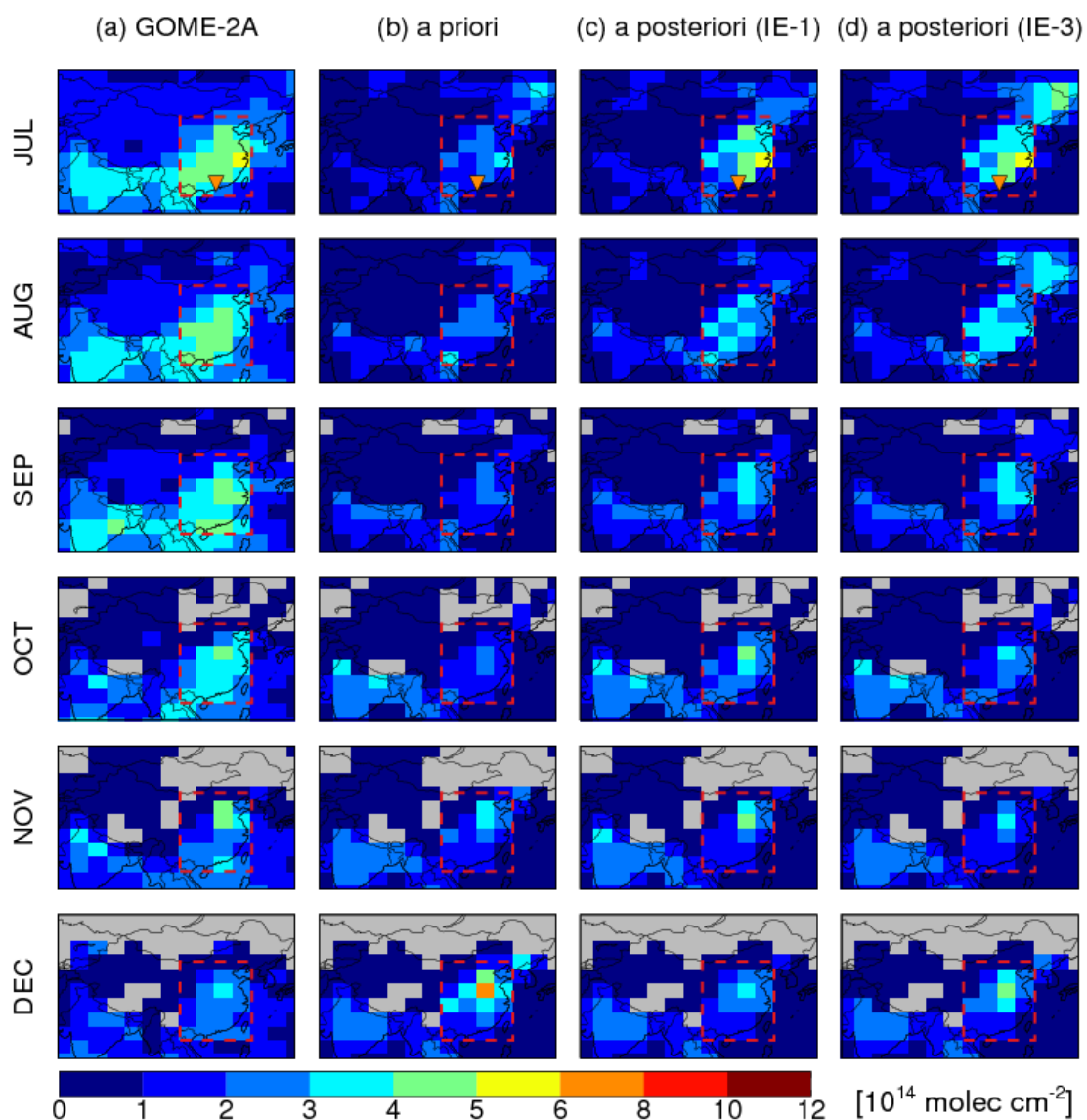


Figure 6. Same as Figure 5 except for July to December. Also shown are ground-based MAX-DOAS measurements at 9:30 local time at Back Garden (July mean, inverted triangles).

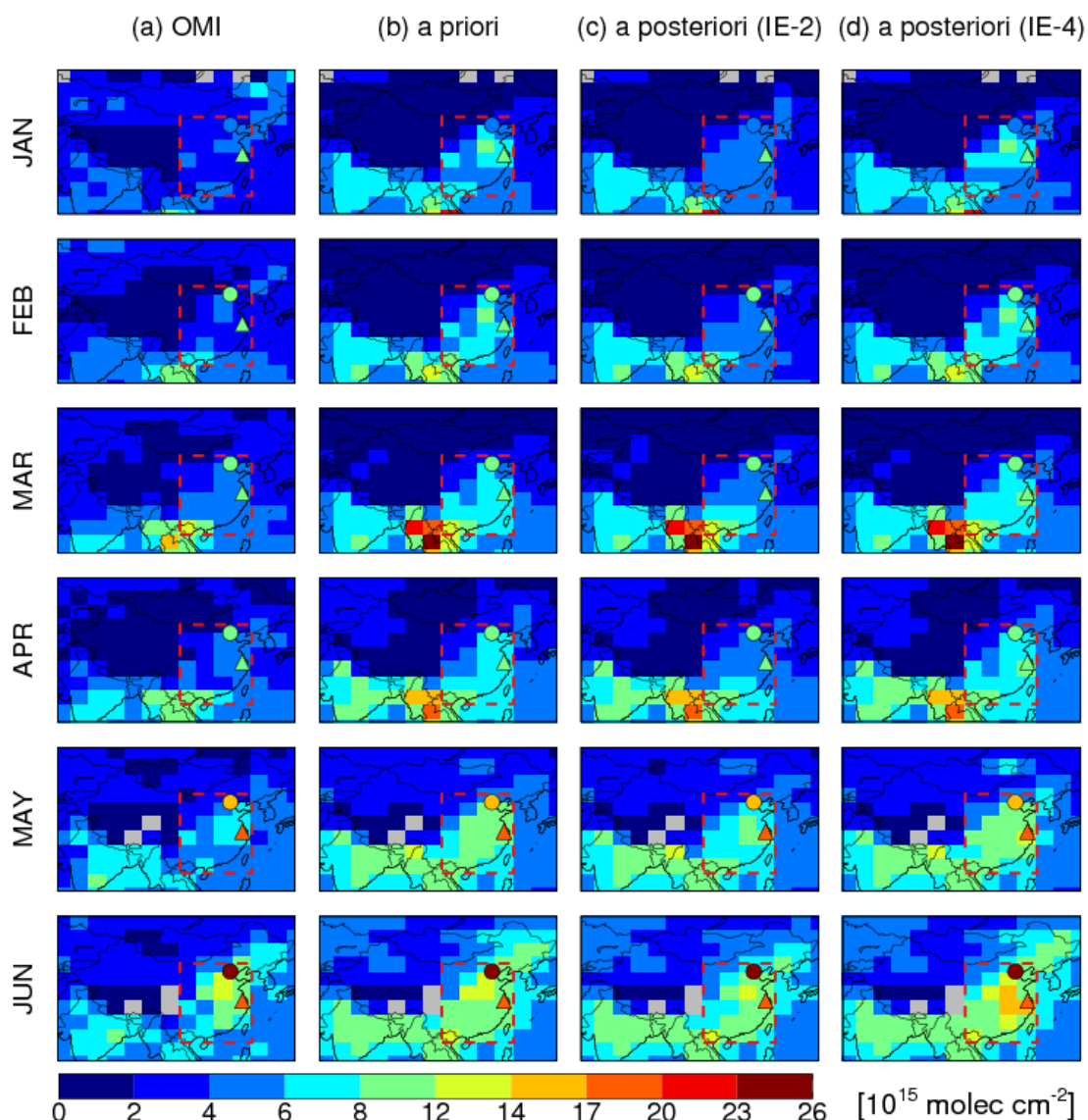


Figure 7. Monthly mean formaldehyde VCDs over China from January to June. For each month, the panels from left to right are: (a) formaldehyde VCDs observed by OMI, (b) formaldehyde VCDs simulated by the model using *a priori* emission estimates, (c) the *a posteriori* formaldehyde VCDs from IE-2, and (d) the *a posteriori* formaldehyde VCDs from IE-4. All model results were sampled at OMI overpass time. Also shown are ground-based MAX-DOAS measurements at 13:30 local time at Xianghe (monthly mean, circles) and Wuxi (bimonthly mean, upward triangles).

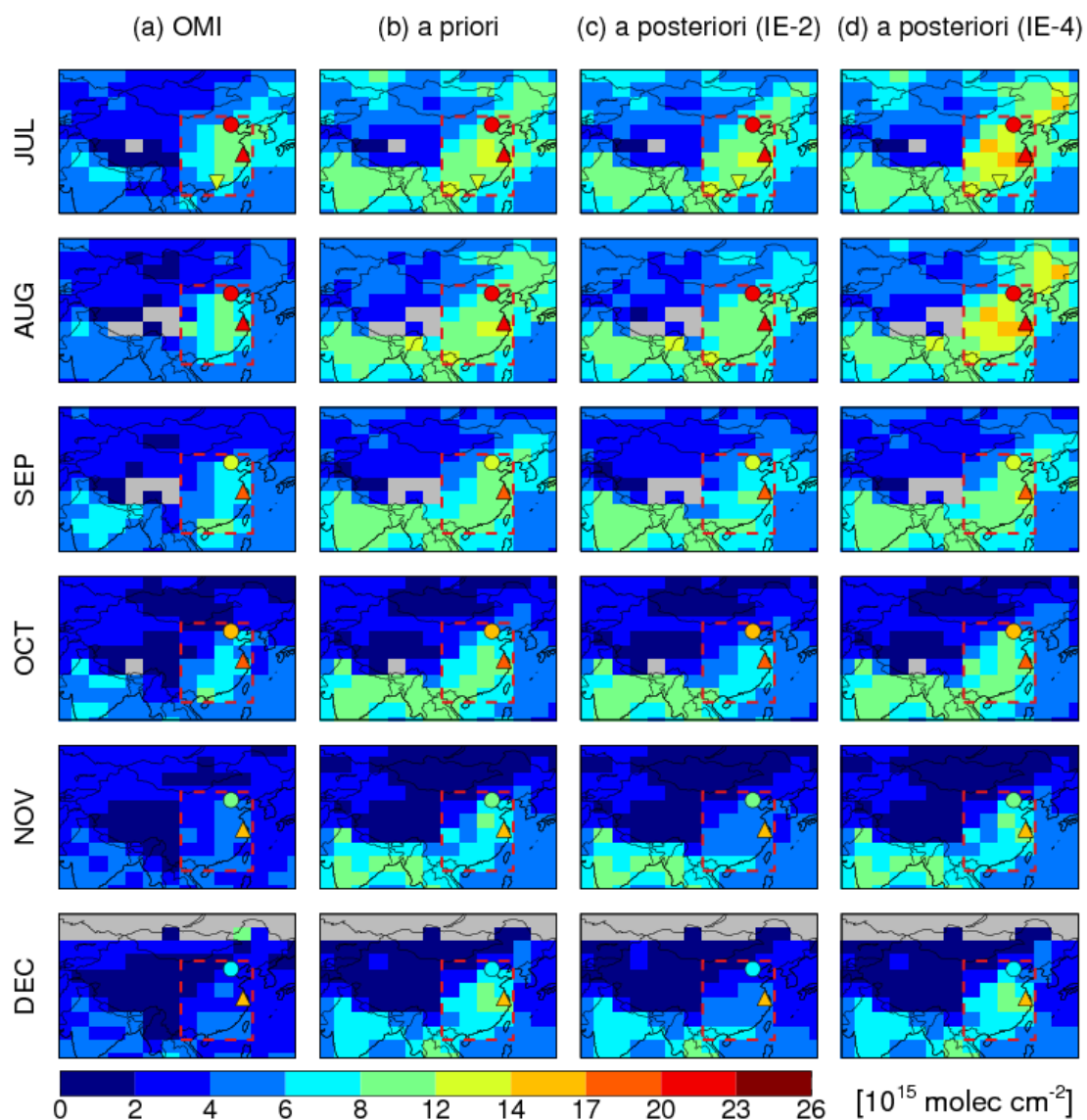


Figure 8. Same as Figure 7 except for July to December. Also shown are ground-based MAX-DOAS measurements at 13:30 local time at Back Garden (July mean, inverted triangles).

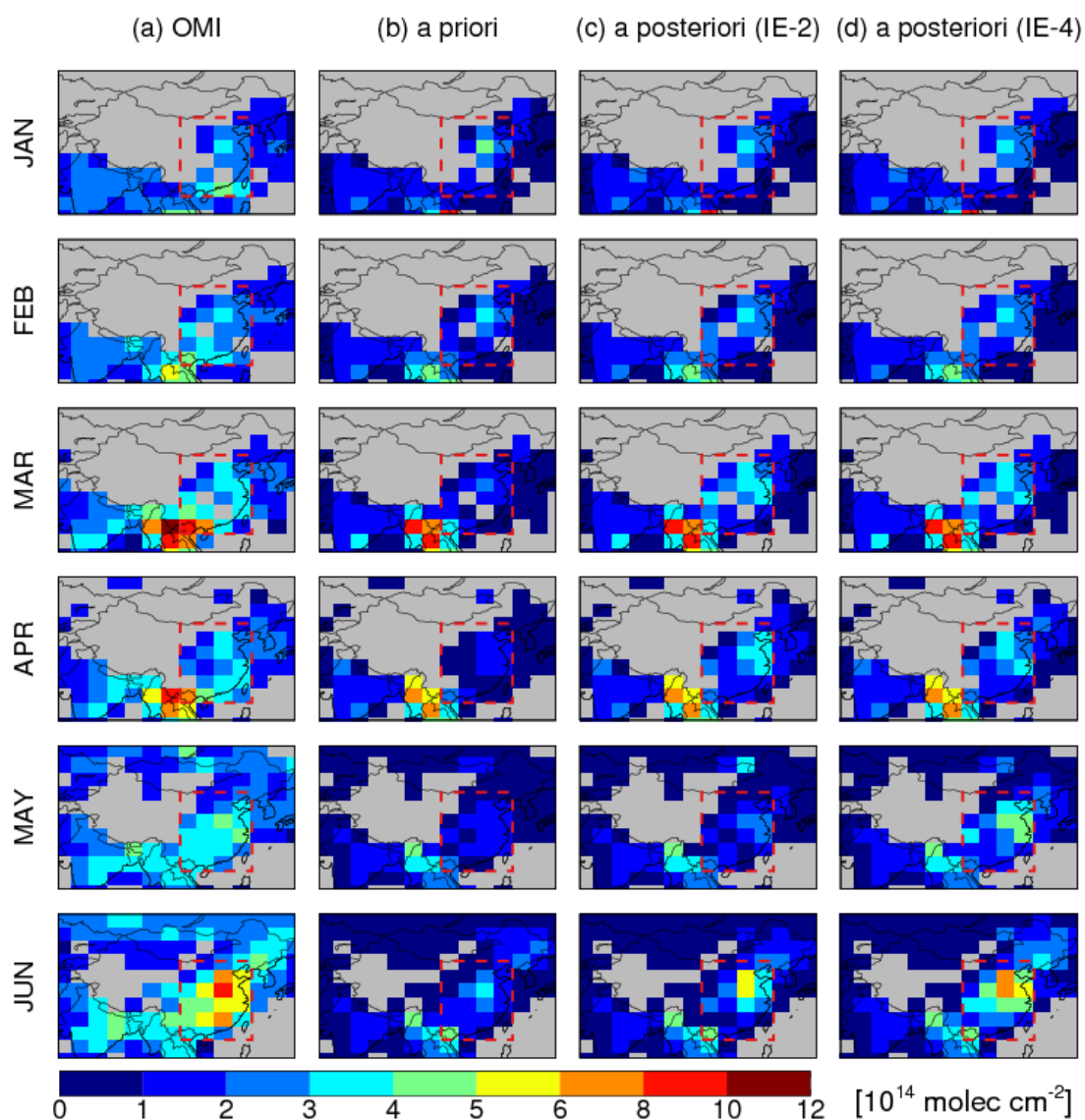


Figure 9. Monthly mean glyoxal VCDs over China from January to June. For each month, the panels from left to right are: (a) glyoxal VCDs observed by OMI, (b) glyoxal VCDs simulated by the model using *a priori* emission estimates, (c) the *a posteriori* glyoxal VCDs from IE-2, and (d) the *a posteriori* glyoxal VCDs from IE-4. All model results were sampled at OMI overpass time.

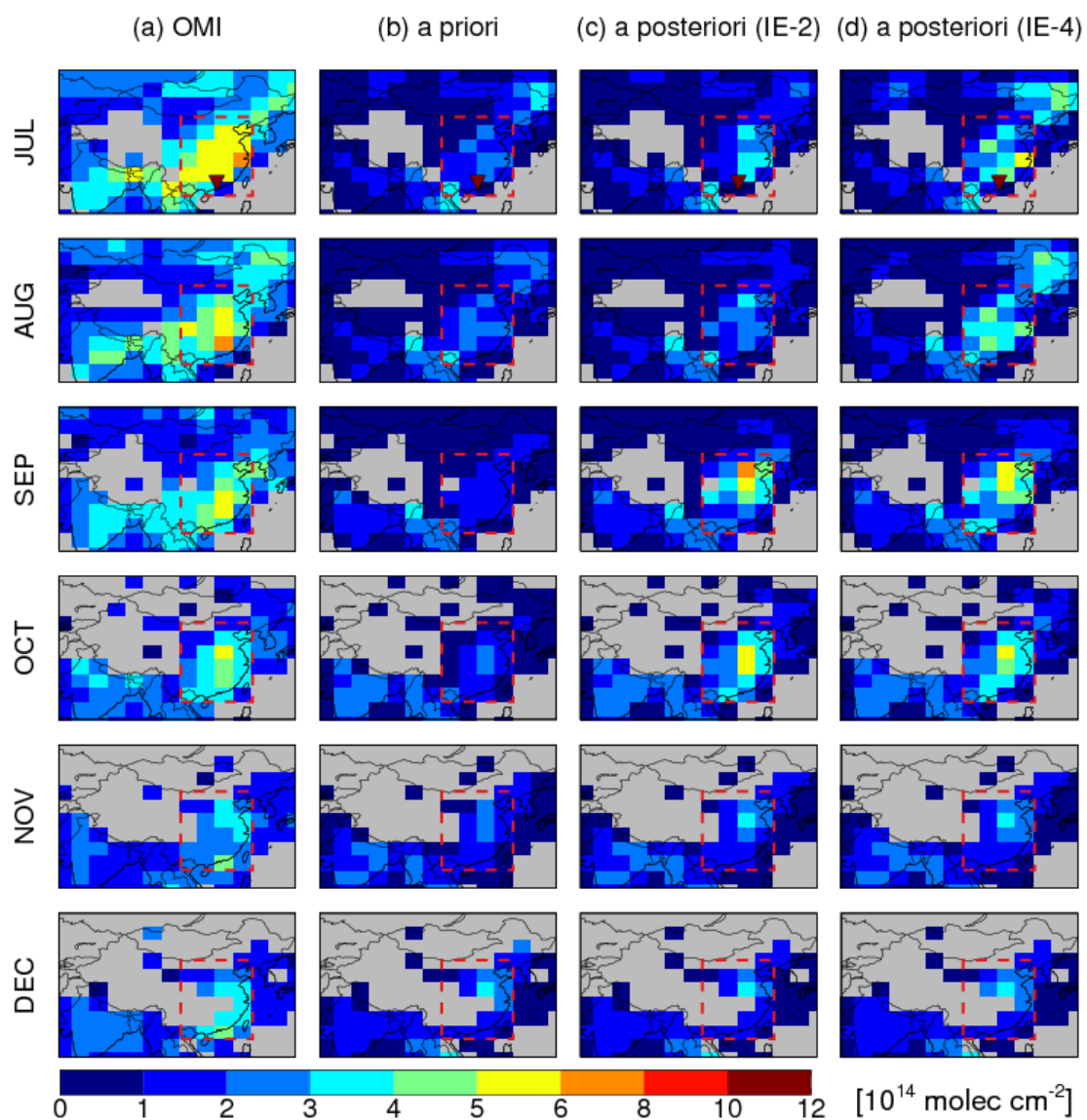
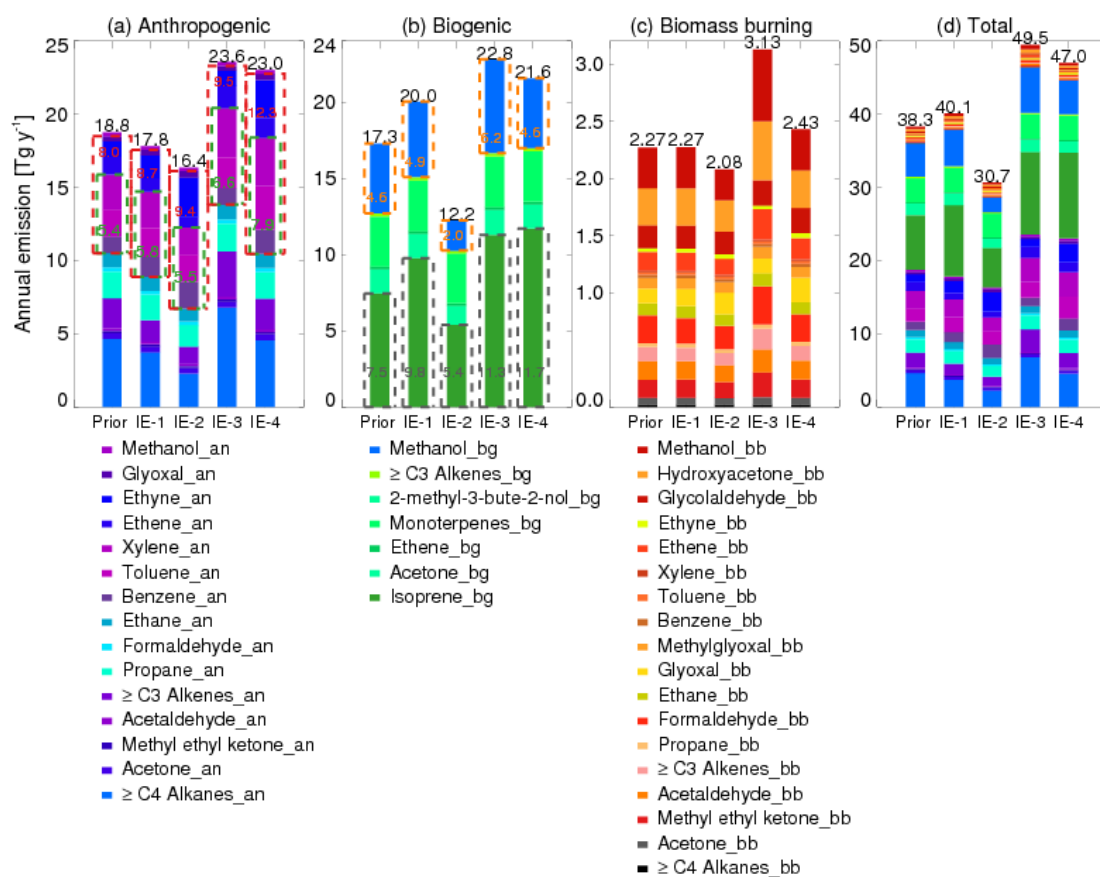


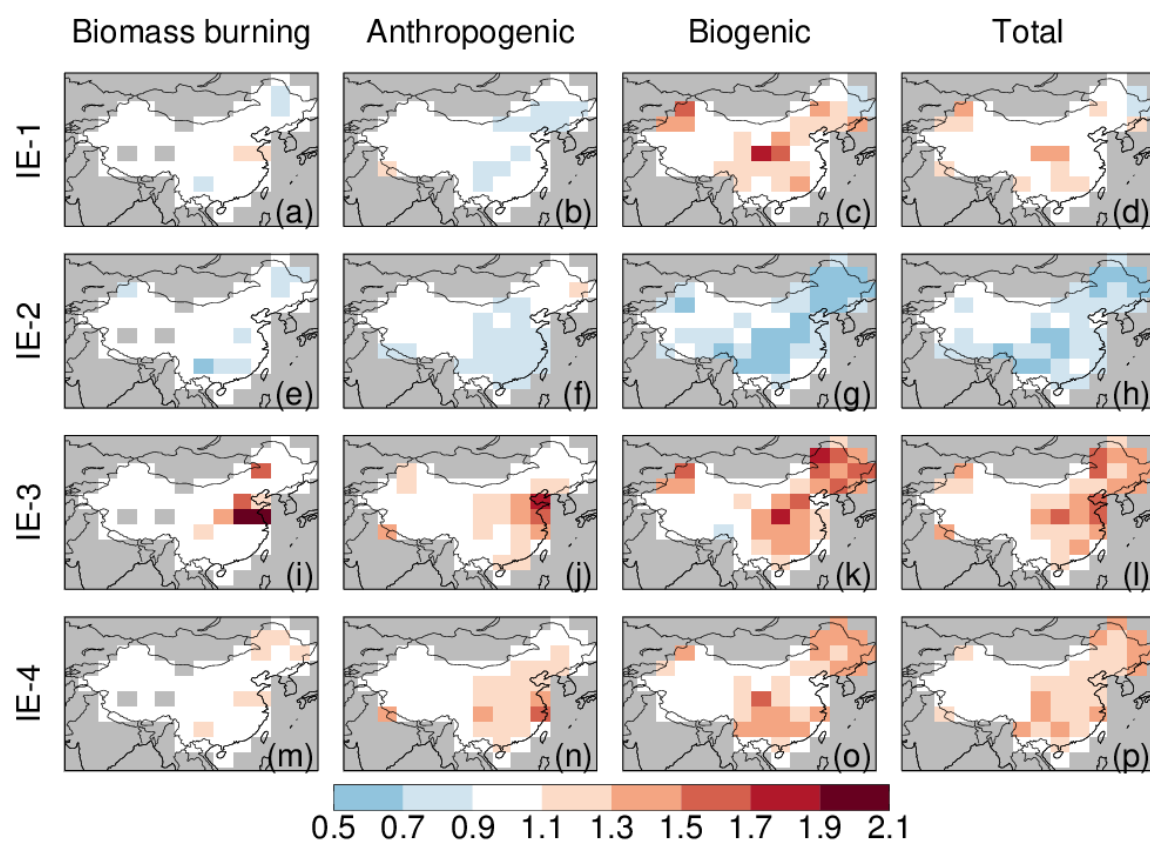
Figure 10. Same as Figure 9 except for July to December. Also shown are ground-based MAX-DOAS measurements at 13:30 local time at Back Garden (July mean, inverted triangles).



1335

1336 **Figure 11. Comparison of estimates of annual Chinese NMVOC emissions from (a) anthropogenic, (b)**
 1337 **biogenic, (c) biomass burning, and (d) total sources. For each panel, the bars from left to right are the *a***
 1338 ***priori* estimates and the *a posteriori* estimates from IE-1, IE-2, IE-3, and IE-4. Annual total NMVOC**
 1339 **emissions are shown in black numbers on top of each bar. The red dashed boxes and red numbers in (a)**
 1340 **indicate annual emissions of anthropogenic glyoxal precursors. The green dashed boxes and green numbers**
 1341 **in (a) indicate annual emissions of anthropogenic aromatics. The grey dashed boxes and grey numbers in (b)**
 1342 **indicate annual biogenic isoprene emissions. The orange dashed boxes and orange numbers in (b) indicate**
 1343 **annual biogenic methanol emissions. Color keys to NMVOC species are shown at the bottom, with suffixes**
 1344 **of ‘an’, ‘bg’, ‘bb’ indicating anthropogenic source, biogenic source, and biomass burning source,**
 1345 **respectively.**

1346

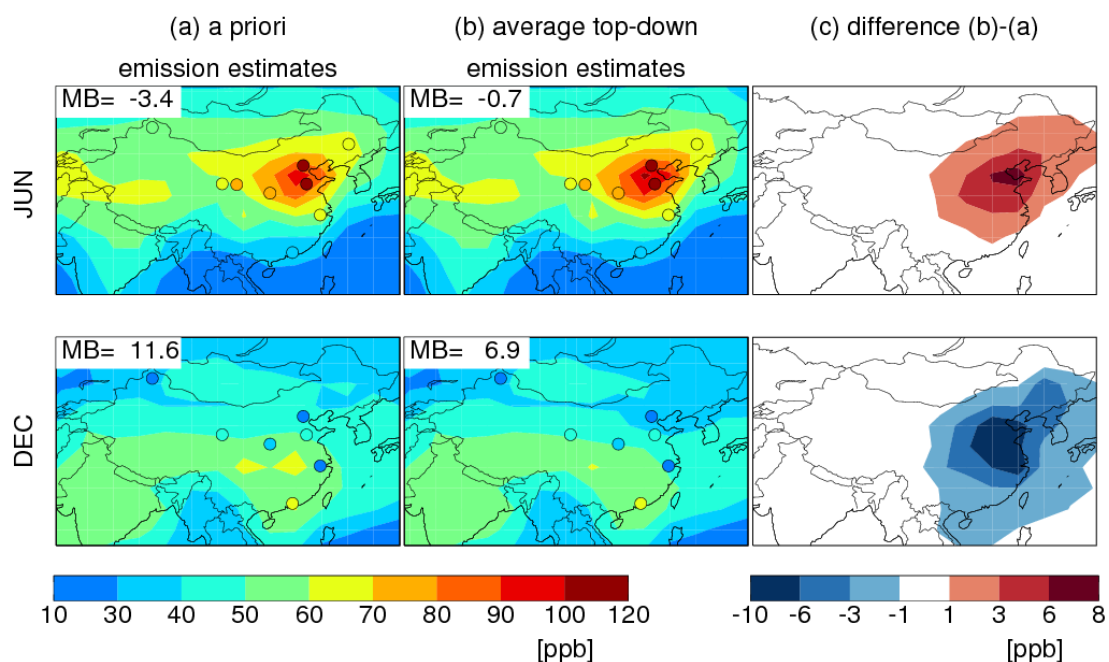


1348

1349 **Figure 12.** Spatial distributions of the optimized scale factors for Chinese annual NMVOC emissions,
 1350 relative to the *a priori* emission estimates, for the four inversion experiments.

1351

1352



1353

1354

1355 **Figure 13. Simulated monthly mean afternoon (13:00-17:00 LT) surface ozone concentrations in June and**1356 **as well as (c) the differences. Filled circles show the afternoon surface ozone observations at several sites in**1357 **China (Table S9). Mean biases (MB) of the simulated concentrations relative to surface measurements are**1358 **shown inset.**

1359

1360

1361

